Ionics
https://doi.org/10.1007/s11581-026-07514-y

RESEARCH

Comparative investigation of the electrochemical performance of Bi_2O_3, PCC, and MWCNT-based composites in a PVDF/DMF matrix for advanced electrode applications

Inci Unlu[1] · Fatma Kilic Dokan[2] · Rifat Battaloglu[1] · Ertugrul Sahmetlioglu[3]

Received: 2 July 2026 / Revised: 4 September 2026 / Accepted: 8 September 2026

Abstract

In this study, Bi_2O_3, precipitated calcium carbonate (PCC), multi-walled carbon nanotube (MWCNT), and ternary Bi_2O_3/PCC/MWCNT-based electrodes were systematically investigated in a PVDF/DMF matrix for supercapacitor applications. Structural, morphological, textural, and electrochemical properties were evaluated using X-ray diffraction (XRD), Fourier transform infrared spectroscopy (FTIR), field-emission scanning electron microscopy (FESEM), Brunauer–Emmett–Teller (BET) analysis, cyclic voltammetry (CV), galvanostatic charge–discharge (GCD), and electrochemical impedance spectroscopy (EIS). Structural characterization confirmed the coexistence of α-Bi_2O_3, calcite PCC, and graphitic MWCNT within the ternary composite, while BET and FESEM analyses revealed an interconnected mesoporous architecture. Among the investigated electrodes, the Bi_2O_3/PCC/MWCNT composite exhibited the highest specific capacitance, reaching 1359.5 F g^{-1} at 1 A g^{-1} and retaining 899.6 F g^{-1} at 10 A g^{-1}, corresponding to a rate retention of 66.2%. In the three-electrode half-cell configuration, an energy density of 196 Wh kg^{-1} was obtained at 1 A g⁻1. EIS analysis further demonstrated a low charge-transfer resistance of 0.87 Ω, supporting improved interfacial charge-transfer kinetics. The enhanced electrochemical response is attributed to the cooperative contributions of redox-active Bi_2O_3, the conductive MWCNT network, and the structurally stabilizing PCC phase. During long-term cycling at 30 A g⁻1, the composite retained 37% of its initial capacitance after 10,000 cycles, exceeding the retention of the Bi_2O_3- and MWCNT-only electrodes but remaining below that of the PCC-only electrode. The principal contribution of this study lies in the incorporation of PCC as a third, structurally stabilizing component into the established Bi_2O_3/MWCNT system, together with the use of an electrospinning-assisted coating approach for electrode fabrication. The results demonstrate that this ternary architecture provides high specific capacitance and favorable rate capability, while further optimization is required to improve its long-term cycling durability.

Keywords Bi_2O_3 · Precipitated calcium carbonate (PCC) · Multi-walled carbon nanotubes (MWCNTs) · Ternary composite electrode · Electrospinning-assisted coating · Supercapacitor

Introduction

The ever-increasing global energy demand, the depletion of fossil fuel resources, and heightened concerns regarding environmental sustainability have emphasized the need for developing high-performance and environmentally friendly energy storage technologies. In this regard, supercapacitors also known as electrochemical capacitors have garnered substantial attention due to their unique advantages, such as long cycle life, high power density, rapid charge/discharge rates, and improved environmental safety when compared to conventional batteries [1–3]. These benefits make supercapacitors highly suitable for next-generation

✉ Rifat Battaloglu
rbattaloglu@ohu.edu.tr

[1] Department of Chemistry, Science Faculty, Niğde Ömer Halisdemir University, Niğde, Türkiye

[2] Department of Chemistry and Chemical Processing Technologies, Mustafa Çıkrıkcıoglu Vocational School, Kayseri University, Kayseri, Türkiye

[3] Department of Basic Sciences of Engineering, Kayseri University, Kayseri, Türkiye

energy systems that require both power efficiency and reliability. The performance of supercapacitors is primarily governed by parameters such as specific energy and power density, cyclic stability, response time, and electrochemical durability, which are intrinsically linked to the properties of electrode materials [4, 5].

Recent advancements in materials science have revealed that composite electrode structures provide a strategic avenue to optimize electrochemical performance. These systems incorporate active materials into conductive polymeric matrices, enabling the development of hybrid architectures that synergistically combine the advantages of different material phases. Among such matrix materials, polymer-based composites especially those based on poly(vinylidene fluoride) (PVDF) have become prominent due to their superior film forming capacity, thermal and chemical stability, cost-effectiveness, and ease of fabrication [6, 7]. PVDF, when dissolved in N,N-dimethylformamide (DMF), facilitates the uniform dispersion of active fillers and enables the formation of continuous and flexible films. However, owing to its electrochemical inertness, PVDF must be integrated with redox-active or conductive components to enhance charge storage capabilities [8–10].

Metal oxides, particularly bismuth oxide (Bi_2O_3), have attracted growing attention as potential pseudocapacitive materials. Bi_2O_3 features a high theoretical specific capacitance (~658 F g^{-1}), is environmentally benign, and exists in several polymorphic crystalline forms that are conducive to redox reactions [11]. Charge storage in Bi_2O_3 primarily involves Faradaic redox processes associated with Bi^{3+}/Bi^0 transitions at the electrode–electrolyte interface. Despite these advantages, Bi_2O_3 suffers from inherently poor electrical conductivity (~10^{-6} S cm^{-1}), limiting its electrochemical rate performance and necessitating hybridization with conductive additives [12].

Multi-walled carbon nanotubes (MWCNTs) are widely employed for this purpose due to their exceptional electrical conductivity (~103 S cm^{-1}), high aspect ratio, large specific surface area (200–400 m2/g), and porous structure-forming ability [13–15]. These features facilitate rapid ion diffusion, efficient charge transfer, and enhanced double-layer capacitance. Moreover, MWCNTs offer mechanical stability, mitigating electrode degradation under repeated cycling. However, MWCNT-only electrodes may suffer from long-term agglomeration or rearrangement under stress, leading to diminished cycling stability [14, 15].

In parallel, precipitated calcium carbonate (PCC) has emerged as a low-cost, environmentally friendly material capable of enhancing porosity and structural integrity when integrated into composite electrodes. PCC contributes to surface area improvement and pore formation, which enhances electrolyte accessibility and ion transport kinetics [16, 17]. Despite its promising physical properties, PCC remains underexplored in supercapacitor applications and is generally not utilized in combination with other active materials.

Although Bi_2O_3/carbon-based binary composites particularly Bi_2O_3/MWCNT systems have been previously investigated to compensate for the intrinsically poor conductivity of Bi_2O_3 [10], such binary architectures generally remain limited by insufficient long-term cycling stability, as the redox-active oxide phase continues to undergo structural degradation and agglomeration during repeated charge–discharge cycling. To address this specific limitation, the present study introduces PCC not as an additional conductive or pseudocapacitive filler, but as a structural stabilizing component that contributes to the distribution of Bi_2O_3 within the conductive MWCNT network and may help mitigate agglomeration. Unlike previously reported Bi_2O_3/CNT electrodes, which typically achieve high initial capacitance at the expense of cycling durability, the present ternary Bi_2O_3/PCC/MWCNT design is specifically engineered to simultaneously preserve high specific capacitance and enhance long-term structural and electrochemical stability, representing a distinct design strategy from conventional binary Bi_2O_3/carbon composites.

In the present study, we systematically investigate the electrochemical behavior of composite electrodes comprising Bi_2O_3, MWCNTs, PCC, and their ternary combinations embedded in a PVDF/DMF matrix. Our results demonstrate that while individual materials contribute distinct functionalities—such as redox activity (Bi_2O_3), electrical conductivity (MWCNTs), and mechanical reinforcement (PCC)— their combination improves overall capacitive performance. This work highlights the importance of rational composite design in achieving electrode architectures with high specific capacitance and favorable rate capability, while further optimization is required to improve long-term cycling durability.

Materıals and methods

Materials

All chemicals and reagents used in this study were of analytical grade and utilized as received without additional purification steps. Bismuth nitrate pentahydrate ($Bi(NO_3)_3 \cdot 5H_2O$, purity ≥ 98%) was obtained from Sigma-Aldrich as the bismuth oxide precursor. Polyvinylidene fluoride (PVDF) powder, also procured from Sigma-Aldrich, served as the polymer matrix. N,N-dimethylformamide (DMF), acetone, ethanol, potassium hydroxide (KOH), hydrochloric acid

(HCl), sodium hydroxide (NaOH), and sodium sulfate (Na_2SO_4) were all sourced from Merck or Sigma-Aldrich, and were employed during synthesis, processing, and electrochemical evaluation stages.

Multi-walled carbon nanotubes (MWCNTs) with an inner diameter range of 0.5–2 nm, outer diameter of 5–15 nm, length of 30–50 µm, and purity exceeding 92%, were used to provide electrical conductivity and structural support in the composite systems.

For electrode fabrication, a TIA-branded electrospinning device was employed. Material dispensing during the electrospinning process was controlled via a TOP-5300 syringe pump manufactured by TOP. Nickel foam sheets (dimensions: 40 mm × 40 mm × 0.08 mm) were obtained from MTIKorea and used as the current collector substrates. Prior to use, the nickel foams were treated with hydrochloric acid for surface activation and thoroughly rinsed with deionized water.

Methods

Synthesis of Bi_2O_3 via hydrothermal method

Bismuth oxide was synthesized using a controlled hydrothermal approach. In a typical procedure, 2 mmol of $Bi(NO_3)_3 \cdot 5H_2O$ and 3 mmol of Na_2SO_4 were dispersed in 40 mL of deionized water and stirred thoroughly. Separately, 18 mmol of NaOH was dissolved in 40 mL of deionized water and added dropwise to the precursor mixture while maintaining continuous agitation. The resulting suspension was sealed in a Teflon-lined stainless steel autoclave and subjected to thermal treatment at 145 °C for 4 h.

Upon cooling to ambient temperature, the yellowish precipitate formed was separated via centrifugation and washed multiple times with deionized water followed by ethanol to remove residual salts and unreacted precursors. The collected solid was dried in an oven at 80 °C for 24 h and subsequently annealed at 450 °C for 2 h to obtain phase-pure crystalline Bi_2O_3 suitable for electrode fabrication (Fig. 1).

Synthesis of Bi_2O_3/PCC/MWCNT nanocomposite via hydrothermal method

Precisely 0.1 g of Bi_2O_3, 0.01 g of PCC, and 0.01 g of MWCNT were combined with 80 mL of distilled water in a Teflon-lined stainless steel autoclave. The mixture was continuously stirred using a magnetic stirrer for 30 min to ensure homogenous dispersion. Subsequently, the autoclave was subjected to hydrothermal treatment at 150 °C for 12 h. The resulting dark gray precipitate was washed several times with distilled water and ethanol to enhance purity. After washing, the sample was dried at 80 °C for 24 h to obtain the nanocomposite powder (Fig. 2).

Preparation of composite mixtures

In this study, four distinct composite mixtures were individually prepared, namely Bi_2O_3/PVDF/DMF, PCC/PVDF/DMF, MWCNT/PVDF/DMF, and a ternary Bi_2O_3/PCC/MWCNT/PVDF/DMF system. N,N-dimethylformamide (DMF) was exclusively selected as the solvent throughout the preparation process, owing to its superior dissolving capability and exceptional compatibility with the polyvinylidene fluoride (PVDF) polymer matrix.

To begin, a PVDF solution with a concentration of 10% (weight/volume) was formulated by the gradual addition of PVDF powder into DMF. This step was conducted under controlled temperature conditions at 60 °C, combined with continuous magnetic stirring to facilitate efficient polymer dissolution. The stirring was prolonged overnight, ensuring complete homogenization and formation of a transparent, uniform solution free from any undissolved particles.

Each active component Bi_2O_3, PCC, MWCNT, or the pre-formed ternary Bi_2O_3/PCC/MWCNT composite powder obtained in Sect. "Synthesis of Bi_2O_3/PCC/MWCNT nanocomposite via hydrothermal method" (fixed internal mass ratio of Bi_2O_3:PCC:MWCNT = 0.1 g: 0.01 g: 0.01 g, i.e., 10:1:1) was separately dispersed as a single filler into a 10 wt% PVDF/DMF polymer solution at a total filler

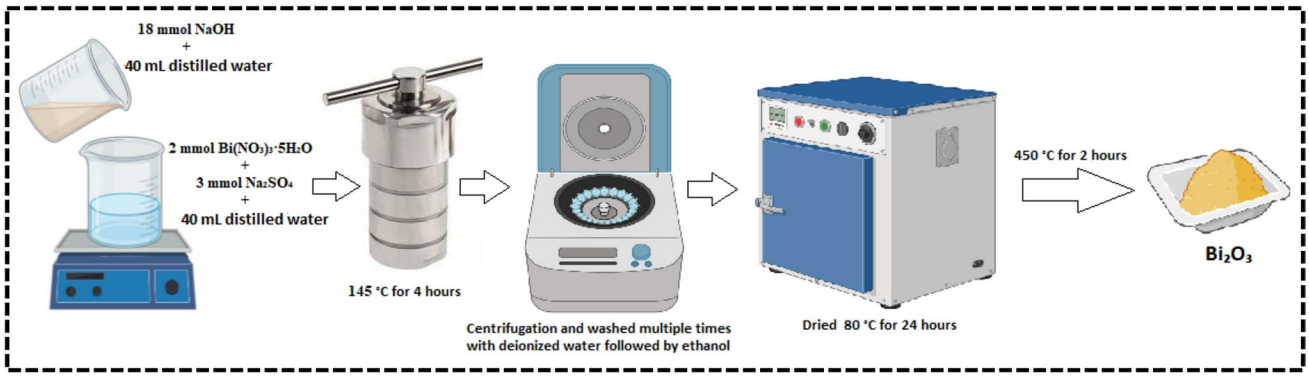

Fig. 1 Schematic representation of the hydrothermal synthesis of Bi_2O_3

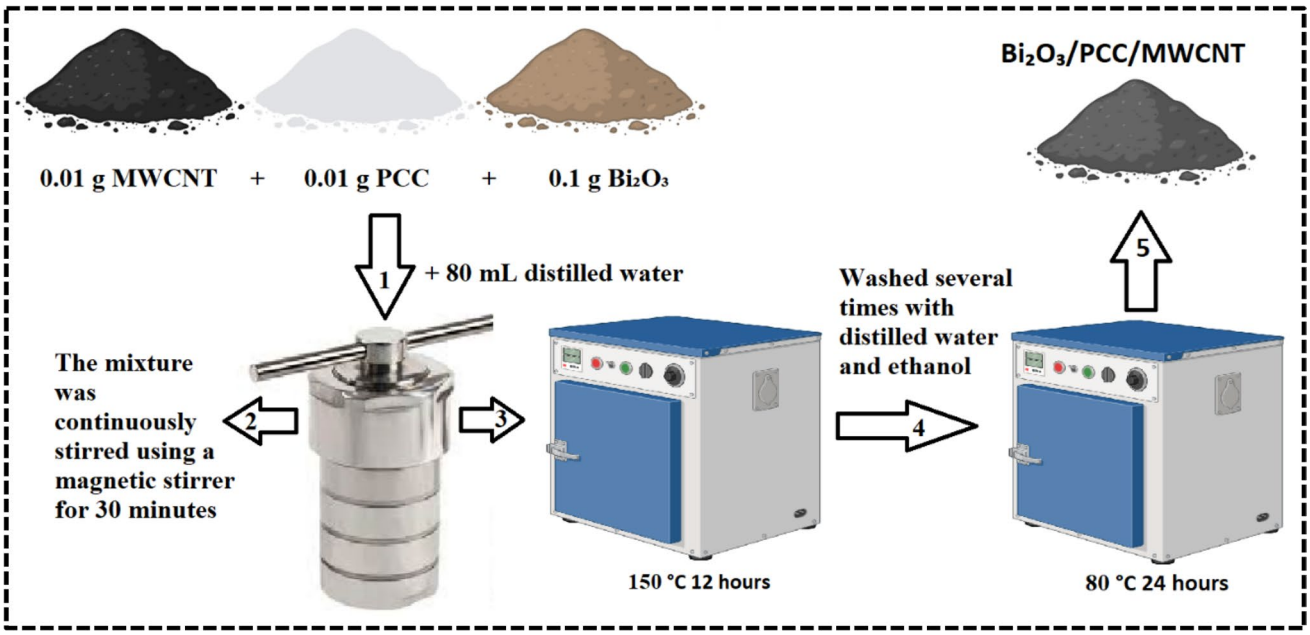

Fig. 2 Schematic representation of the hydrothermal synthesis of the Bi_2O_3/PCC/MWCNT nanocomposite

loading of 1 wt%. This loading therefore refers to the total mass of active filler relative to the polymer solution in each case, and is identical whether the filler is a single component (Bi_2O_3, PCC, or MWCNT alone) or the ternary composite powder as a whole, rather than corresponding to 1 wt% of each individual component within the ternary system. The mixtures were first treated in an ultrasonic bath and then stirred overnight using a magnetic stirrer. This procedure ensures uniform and homogeneous dispersion of the fillers within the polymer matrix, which is critical for optimizing the electrochemical performance of the resulting composite electrodes.

Electrospinning assisted coating

The four distinct composite solutions Bi_2O_3/PVDF/DMF, PCC/PVDF/DMF, MWCNT/PVDF/DMF, and the ternary Bi_2O_3/PCC/MWCNT/PVDF/DMF system were individually processed via electrospinning. This technique enables the controlled and continuous transformation of polymer solutions into nanofibers, resulting in high surface area and porous structures on the electrode surface. Throughout the experiments, the feed rate was maintained constant at 3 mL/h to ensure stable solution delivery. For uniform and efficient fiber collection, nickel foam substrates were precisely fixed onto a rotating drum, with the distance between the needle tip and the rotating drum strictly maintained at 12 cm. Maintaining this fixed gap optimized the electrostatic forces involved in fiber formation and deposition, facilitating the creation of homogeneous and orderly fiber mats.

The applied voltage was adjusted individually for each formulation because differences in filler composition resulted in variations in electrospinning behavior. During preliminary trials, the voltage was varied in small increments until a stable Taylor cone, continuous jet formation, and uniform deposition were achieved without visible dripping or jet instability. Based on these observations, voltages of 12.78 kV, 11.89 kV, 9.06 kV, and 9.41 kV were selected for the Bi_2O_3/PVDF/DMF, PCC/PVDF/DMF, MWCNT/PVDF/DMF, and ternary Bi_2O_3/PCC/MWCNT/PVDF/DMF formulations, respectively. These values therefore represent empirically selected stable operating conditions rather than the results of a separate systematic voltage-optimization study. Throughout this procedure, the other electrospinning parameters, including the feed rate (3 mL $h^{-}1$) and needle-to-collector distance (12 cm), were kept constant. Under these conditions, continuous and porous electrospun coatings were deposited onto the nickel foam substrates. After deposition, the coated substrates were dried and subsequently prepared for electrochemical testing and further characterization.

Structural characterization

The structural characteristics of Bi_2O_3, PCC, MWCNT, and the Bi_2O_3/PCC/MWCNT composite were systematically examined using X-ray diffraction (XRD), Fourier transform infrared spectroscopy (FTIR), nitrogen adsorption–desorption measurements (BET), field-emission scanning electron microscopy (FESEM), and energy-dispersive X-ray spectroscopy (EDS) elemental mapping. XRD analysis was employed to identify the crystalline phases and to verify the

successful formation of Bi_2O_3 along with the effective integration of PCC and MWCNT within the composite matrix. FTIR spectroscopy was utilized to elucidate the characteristic vibrational features and functional groups associated with each constituent material. FESEM was used to investigate the surface morphology and microstructural features of the individual materials and ternary composite, while EDS elemental mapping was employed to evaluate the spatial distribution of the constituent elements within the composite and to provide additional evidence for the coexistence of the component phases. BET analysis was used to evaluate the specific surface area and pore characteristics of the investigated materials.

Electrochemical characterization

Electrode fabrication Nickel foams, chosen for their high surface area and excellent electrical conductivity, were carefully cut into dimensions of 14 mm × 10 mm to prepare the working electrodes suitable for electrochemical applications. To eliminate surface oxides and contaminants that could impede interfacial conductivity, the foams were immersed in a 1 M hydrochloric acid (HCl) solution for a short duration. Following acid treatment, they were thoroughly rinsed with deionized water and dried at room temperature. This surface treatment was essential to ensure improved adhesion of the active layer and enhance the overall electrochemical response through better contact between the active material and the current collector.

For electrospinning assisted coating, the cleaned nickel foams were securely fixed onto a rotating drum within the electrospinning apparatus. A 10% (w/v) PVDF/DMF-based polymer solution, prepared with the appropriate active filler, was then applied onto the foam surfaces using the electrospinning assisted coating technique. This method allowed the formation of a uniform and continuous layer of polymer across the porous substrate, facilitating optimal integration of the electroactive phase. The electrospinning assisted coating PVDF layer promoted structural coherence while enabling adequate exposure of the foam's porosity, which is beneficial for ion transport during charge–discharge cycles.

After coating, the electrodes were subjected to a vacuum drying process at 80 °C for 12 h to completely evaporate residual solvent and to stabilize the deposited layer. The total mass of the active material deposited on each nickel foam was approximately 1 mg, a value later used for normalization in specific capacitance and electrochemical performance calculations.

Electrochemical evaluation of the electrodes The electrochemical properties of the prepared electrodes were systematically examined using a Gamry Reference 3000 electrochemical workstation. All measurements were conducted in a conventional three-electrode configuration**.** The composite-coated nickel foams served as the working electrodes, while an Ag/AgCl electrode was employed as the reference electrode, and a platinum foil (1 cm × 1 cm) was used as the counter electrode.

All electrochemical tests were performed in a highly conductive 2 M KOH aqueous solution**.** This experimental setup enabled a reliable assessment of the electrodes' charge storage capabilities, electrical conductivity, and cycling stability. The data collected from these tests facilitated a comparative evaluation of the different electrode compositions and offered valuable insights into their potential suitability for high-performance supercapacitor applications.

Specific capacitance (C_s, F g^{-1}) was calculated from the galvanostatic discharge curves using the following equation:

$$C_s = (I \times \Delta t)/(m \times \Delta V) \quad (1)$$

where I is the applied discharge current (A), Δt is the discharge time (s), m is the mass of the active material loaded on the electrode (g), and ΔV is the potential window (V), excluding the IR drop.

Energy density (E, Wh kg^{-1}) and power density (P, W kg^{-1}) were subsequently derived from the specific capacitance values as follows:

$$E = (C_s \times \Delta V^2)/(2 \times 3.6) \quad (2)$$

$$P = (E \times 3600)/\Delta t \quad (3)$$

All specific capacitance, energy density, and power density values reported in this study were normalized to the mass of the active material alone (~1 mg per electrode, Sect. "Electrode fabrication") and correspond to a three-electrode half-cell configuration (working electrode vs. Ag/AgCl reference, Pt counter electrode) in 2 M KOH electrolyte. As these values are not normalized to the total mass of a packaged, two-electrode device, they are inherently higher than those typically obtained for a practical full-cell configuration, consistent with common practice in the supercapacitor literature.

Results and discussion

Characterization results

The XRD pattern of the Bi_2O_3 sample exhibits sharp and well-defined diffraction peaks, indicating a high degree of crystallinity. The major reflections observed at $2\theta \approx 27.4°$, 33.1°, 46.3°, and 55.5° can be indexed to the (120), (121),

Table 1 Indexed diffraction peaks of Bi_2O_3, PCC, and MWCNT

Sample	2θ (°)	(hkl)	Phase	JCPDS No.	Ref.
Bi_2O_3	27.4	(120)	α-Bi_2O_3	41–1449	[19]
Bi_2O_3	33.1	(121)	α-Bi_2O_3	41–1449	[19]
Bi_2O_3	46.3	(041)	α-Bi_2O_3	41–1449	[19]
Bi_2O_3	55.5	(240)	α-Bi_2O_3	41–1449	[19]
PCC ($CaCO_3$)	29.4	(104)	Calcite	05–0586	[20]
PCC ($CaCO_3$)	39.4	(113)	Calcite	05–0586	[20]
PCC ($CaCO_3$)	43.1	(202)	Calcite	05–0586	[20]
PCC ($CaCO_3$)	47.5	(018)	Calcite	05–0586	[20]
MWCNT	26.0	(002)	Graphitic carbon	41–1487	[21]

(041), and (240) planes of monoclinic α-Bi_2O_3 (JCPDS No. 41–1449) [18], confirming the successful formation of the α-Bi_2O_3 phase without detectable impurity phases. The PCC sample shows intense diffraction peaks located at 2θ ≈ 29.4°, 39.4°, 43.1°, and 47.5°, corresponding to the (104), (113), (202), and (018) planes of calcite $CaCO_3$ (JCPDS No. 05–0586) (Table 1) (Fig. 3) [20].

The MWCNT sample presents a broad peak at around 2θ ≈ 26°, assigned to the (002) plane of graphitic carbon (JCPDS No. 41–1487) (Table 1). The composite sample contains the characteristic peaks of α-Bi_2O_3 and PCC together with the carbon-related reflection of MWCNT, indicating successful composite formation without altering the primary crystal structure.

To provide a quantitative assessment of the crystalline domains, the crystallite dimensions of the individual components were estimated from selected characteristic reflections using the Scherrer equation, $D = K\lambda/(\beta\cos\theta)$, where D is the crystallite size, K is the shape factor (0.9), λ is the wavelength of Cu Kα radiation (1.5406 Å), β is the full width at half maximum (FWHM) of the selected diffraction peak in radians, and θ is the corresponding Bragg angle. The calculated XRD-derived structural parameters are summarized in Table 2.

As shown in Table 2, the characteristic Bi_2O_3 and PCC reflections yielded crystallite sizes of approximately 82.2 and 80.5 nm, respectively. For MWCNT, the broad graphitic (002) reflection centered at 25.716° corresponds to an interlayer spacing d002 of 3.4615 Å and a coherent stacking height Lc of approximately 2.84 nm. The Lc value represents the coherent stacking dimension of the graphitic layers and should not be interpreted as the physical nanotube diameter. A single Scherrer crystallite-size value was not assigned to the ternary Bi_2O_3/PCC/MWCNT composite because its diffraction pattern contains overlapping reflections from multiple crystalline phases; therefore, the structural characteristics of the composite were evaluated separately by multiphase Rietveld refinement.

Rietveld refinement was further employed to quantitatively evaluate the crystallographic characteristics of the individual components and the corresponding crystalline phases within the ternary composite. As summarized in Table 3, monoclinic Bi_2O_3 exhibited refined lattice parameters of a = 5.84638 Å, b = 8.16806 Å, c = 7.51431 Å, and β = 112.9937°. In the ternary composite, the corresponding Bi_2O_3 phase showed slightly modified

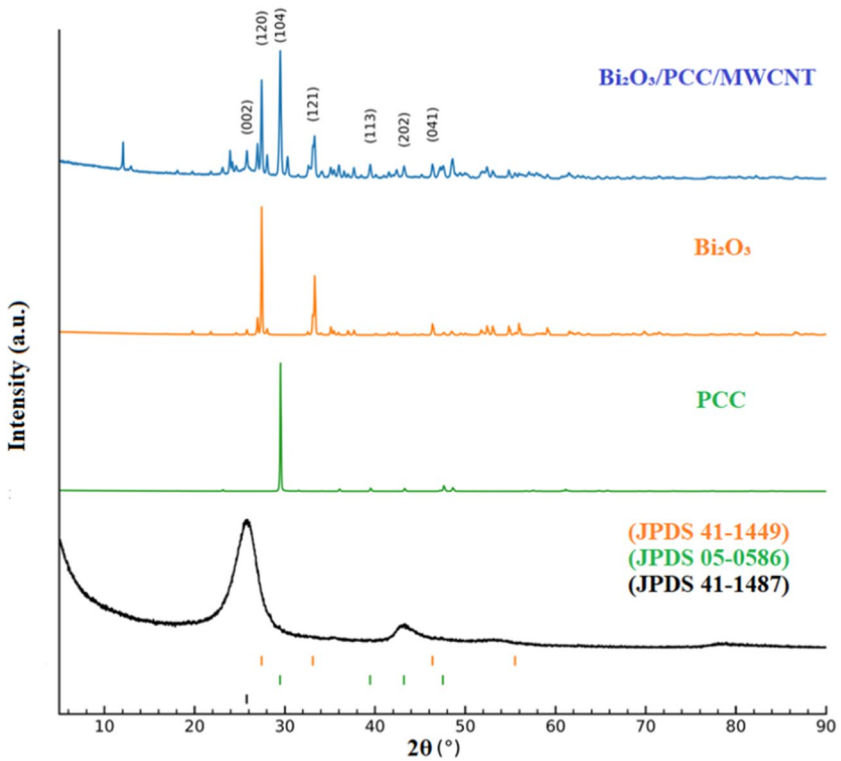

Fig. 3 X-ray diffraction (XRD) patterns of Bi_2O_3, PCC, MWCNT, and Bi_2O_3/PCC/MWCNT composite samples

Table 2 XRD-derived structural parameters and crystallite dimensions of the pristine components

Sample	Selected reflection (hkl)	2θ (°)	FWHM (°)	d-spacing (Å)	Crystallite size/Lc (nm)
Bi_2O_3	(120)	27.4195	0.0995	3.2502	82.2
PCC	(104)	29.4948	0.1021	3.0260	80.5
MWCNT	(002)	25.716	2.874	3.4615	2.84 (Lc)

Table 3 Rietveld-refined crystallographic parameters of the individual components and corresponding phases in the ternary composite

Sample/phase	a (Å)	b (Å)	c (Å)	α (°)	β (°)	γ (°)
Bi_2O_3	5.84638	8.16806	7.51431	90	112.9937	90
Bi_2O_3 phase in composite	5.85033	8.17128	7.51484	90	113.0138	90
PCC ($CaCO_3$)	4.98654	4.98654	17.04504	90	90	120
PCC phase in composite	4.99095	4.99095	17.04368	90	90	120
MWCNT	2.59340	2.59340	7.24856	90	90	120

values of a = 5.85033 Å, b = 8.17128 Å, c = 7.51484 Å, and β = 113.0138°. Similarly, the PCC phase exhibited a = b = 4.98654 Å and c = 17.04504 Å, whereas the corresponding phase in the composite showed a = b = 4.99095 Å and c = 17.04368 Å. These relatively small variations indicate that the principal crystalline frameworks of Bi_2O_3 and PCC are largely preserved following composite formation, while the minor changes in the refined lattice parameters may reflect slight lattice distortion associated with interactions among the constituent phases. The MWCNT phase exhibited hexagonal lattice parameters of a = b = 2.59340 Å and c = 7.24856 Å. Overall, the refinement results support the coexistence and structural retention of the constituent crystalline phases in the ternary composite without evidence of a major crystallographic transformation.

The FTIR spectra of Bi_2O_3, PCC, MWCNT, and the Bi_2O_3/PCC/MWCNT composite are presented in Fig. 4, with the characteristic absorption bands directly annotated on the spectra to facilitate comparison. The Bi_2O_3 spectrum exhibits several characteristic absorption bands in the low-wavenumber region at 536.09, 498.63, 478.90, and 426.30 cm^{-1}, which are associated with Bi–O lattice vibrations [22]. Additional bands are observed at 2918.7, 2852.7, and 1416.7 cm^{-1}.

The PCC spectrum displays a strong carbonate absorption band at 1416.5 cm^{-1}, together with characteristic bands at 875.73 and 711.23 cm^{-1}, corresponding to the vibrational modes of the CO_3^{2-} group in calcite-type $CaCO_3$ [23]. Additional bands are observed at 1796.2, 496.44, and 478.90 cm^{-1}. The MWCNT spectrum exhibits bands at 3665.9, 2923.1, 2852.7, 1740.0, 1072.9, 898.15, 871.23, 722.19, 527.12, and 454.79 cm^{-1}. Among these, the bands in the 2923–2853 cm^{-1} region are associated with C–H stretching vibrations, while the bands at 1740.0 and 1072.9 cm^{-1} are consistent with oxygen-containing surface functionalities [24, 25].

The FTIR spectrum of the Bi_2O_3/PCC/MWCNT composite contains characteristic contributions from the constituent materials, with bands observed at 2918.7, 2848.4, 1415.7, 1070.7, 873.42, 711.23, and 439.45 cm^{-1}. Importantly,

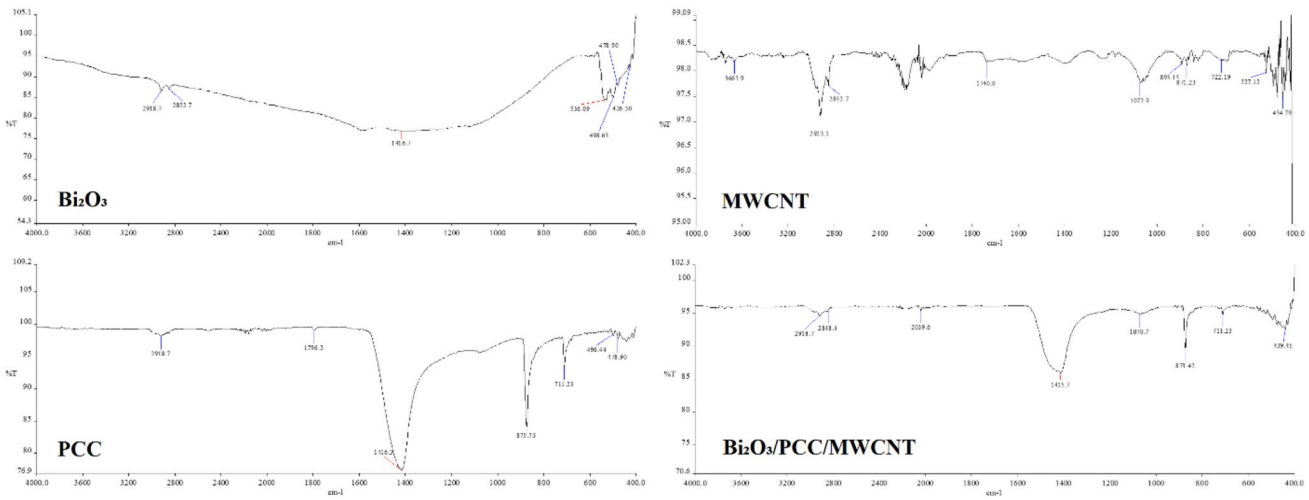

Fig. 4 FTIR spectra of Bi_2O_3, MWCNT, PCC, and the Bi_2O_3/PCC/MWCNT ternary composite. The labeled absorption bands indicate the characteristic vibrational features of the individual components and allow comparison of the corresponding band positions and shifts observed after composite formation

comparison with the pristine components reveals small but measurable changes in selected vibrational frequencies. The characteristic PCC carbonate band at 1416.5 cm^{-1} shifts to 1415.7 cm^{-1} in the composite ($\Delta\nu = -0.80$ cm^{-1}), while the band at 875.73 cm^{-1} shifts to 873.42 cm^{-1} ($\Delta\nu = -2.31$ cm^{-1}). In contrast, the carbonate band at 711.23 cm^{-1} remains essentially unchanged ($\Delta\nu = 0.00$ cm^{-1}). Similarly, the MWCNT-associated band at 1072.9 cm^{-1} shifts to 1070.7 cm^{-1} in the composite ($\Delta\nu = -2.20$ cm^{-1}). These relatively small shifts indicate subtle changes in the local vibrational environments of the carbonate and carbon-containing functionalities following composite formation and are consistent with interfacial interactions among the constituent phases. However, because the observed shifts are small, they are interpreted as evidence of changes in the local chemical environment rather than as proof of the formation of new chemical bonds or a new bulk chemical phase. Overall, the preservation of the principal characteristic bands indicates that the fundamental chemical structures of the individual components are largely retained after formation of the ternary composite.

Brunauer–Emmett–Teller (BET) surface area and textural parameters of Bi_2O_3, PCC, MWCNT, and the Bi_2O_3/PCC/MWCNT composite were determined from N_2 adsorption–desorption measurements (Fig. 5). The nitrogen adsorption–desorption results reveal pronounced differences in the textural properties of the prepared materials. MWCNT exhibits the highest BET surface area (SBET = 176.17 m^2 g^{-1}) and the largest total pore volume (Vt = 0.9593 cm^3 g^{-1}), which is consistent with the intrinsically porous and high-surface-area nature of carbon nanotube networks [26–28]. The ternary Bi_2O_3/PCC/MWCNT composite

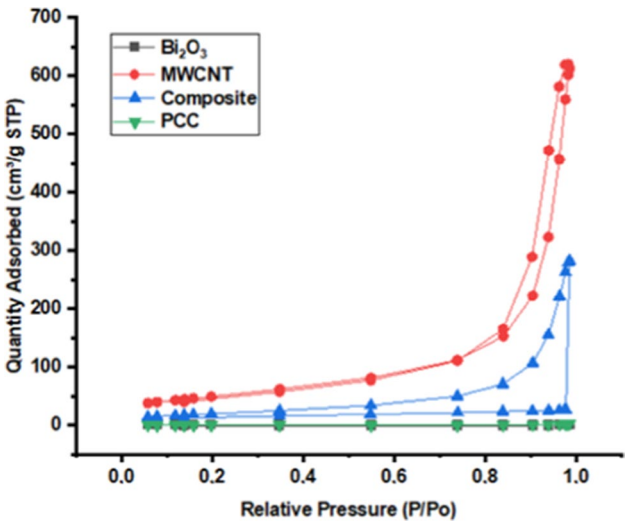

Fig. 5 BET nitrogen adsorption–desorption isotherms of Bi_2O_3, PCC, MWCNT, and Bi_2O_3/PCC/MWCNT composite materials recorded at 77 K

shows a markedly enhanced surface area (SBET = 71.21 m^2 g^{-1}) and pore volume (Vt = 0.4377 cm^3 g^{-1}) compared with the oxide- and carbonate-only samples, indicating that the incorporation of MWCNT significantly contributes to the development of accessible porosity within the composite framework. In contrast, Bi_2O_3 and PCC exhibit very low surface areas (0.73 and 0.79 m^2 g^{-1}, respectively), suggesting limited accessible porosity.

The average pore diameters, calculated using the relation 4Vt/SBET, fall within the mesoporous range (≈16–28 nm) for all samples, confirming the predominance of mesopore-dominated textures. Overall, the composite material achieves a balanced textural profile, with intermediate surface area and pore volume relative to MWCNT, which is favorable for electrolyte penetration and efficient ion transport in electrochemical applications. To more directly relate these textural parameters to the electrochemical results, the specific capacitance values were normalized to the corresponding SBET of each electrode, yielding area-normalized capacitances of approximately 1374, 1173, 6.9, and 19.1 F m^{-2} for Bi_2O_3, PCC, MWCNT, and the composite, respectively. The markedly higher area-normalized capacitance of the composite compared with MWCNT indicates that its charge storage cannot be explained by surface-area-scaled, double-layer-type charging alone: if the composite behaved as a purely double-layer capacitor with the same area-specific capacitance as MWCNT, its SBET of 71.21 m^2 g^{-1} would be expected to yield only ≈494 F g^{-1}, well below the 1359.5 F g^{-1} actually measured. This discrepancy provides quantitative textural evidence, complementary to the EIS results, that the additional capacitance originates from the redox-active Bi_2O_3 phase rather than from surface area effects. Furthermore, despite possessing roughly 2.5-fold lower surface area than MWCNT, the composite exhibits both a lower charge-transfer resistance (Rct = 0.87 Ω vs. 1.23 Ω) and a lower Warburg coefficient (0.52 vs. 0.74 $\Omega \cdot s^{-0.5}$), indicating that its intermediate pore volume (Vt = 0.4377 cm^3 g^{-1}) and mesopore-dominated architecture (Davg ≈ 24.6 nm) provide sufficiently accessible ion-transport pathways without requiring the maximum surface area. This is further corroborated by the capacitance retention from 1 to 10 A g^{-1}, where the composite achieves the highest retention (66.2%) among all electrodes, marginally exceeding even MWCNT (65.2%), suggesting that beyond a sufficiently interconnected mesoporous network, further increases in surface area offer diminishing returns for high-rate ion accessibility (Table 4).

The N_2 adsorption–desorption isotherms of Bi_2O_3, PCC, MWCNT, and the Bi_2O_3/PCC/MWCNT composite are presented in Fig. 5. According to the IUPAC classification, all samples exhibit type IV isotherms [29], indicating the

Table 4 BET textural parameters

Sample	SBET ($m^2 g^{-1}$)	Vt ($cm^3 g^{-1}$)	Davg (nm)	C
Bi_2O_3	0.73	0.0029	16.17	18.92
PCC	0.79	0.0055	27.85	65.24
MWCNT	176.17	0.9593	21.78	110.39
Bi_2O_3/PCC/MWCNT (Composite)	71.21	0.4377	24.59	51.53

presence of a mesoporous structure. The relatively low adsorption uptake at low relative pressures ($P/P_0 < 0.1$) suggests a limited contribution from micropores, whereas the pronounced increase in nitrogen adsorption at higher relative pressures ($P/P_0 > 0.6$) can be attributed to capillary condensation within mesopores.

Among the investigated materials, MWCNT shows the highest nitrogen adsorption capacity over the entire pressure range, reflecting its large specific surface area and well-developed porous network. In contrast, pristine Bi_2O_3 displays significantly lower adsorption, indicative of a denser morphology with limited accessible surface area. PCC also exhibits relatively low adsorption, implying a less porous structure. These BET results are in good agreement with the FESEM observations [30]. The FESEM images reveal that pristine Bi_2O_3 exhibits a relatively compact and agglomerated morphology, consistent with its low nitrogen adsorption capacity. PCC shows a dense structure with limited visible porosity, further supporting its low surface area. In contrast, MWCNT displays an interconnected tubular network, providing abundant open channels and a highly accessible surface, which explains its superior adsorption behavior [31].

Notably, the Bi_2O_3/PCC/MWCNT composite presents a more homogeneous and porous morphology, where Bi_2O_3 particles are uniformly distributed and anchored onto the MWCNT framework with the assistance of PCC. This interconnected architecture creates open pathways for electrolyte diffusion and increases the number of accessible electroactive sites. Such morphological features observed by FESEM corroborate the mesoporous characteristics inferred from the BET analysis and highlight the complementary structural contributions of the composite [32].

The Bi_2O_3/PCC/MWCNT composite demonstrates a substantially higher adsorption capacity compared to Bi_2O_3 and PCC, though slightly lower than that of MWCNT. This enhancement is mainly associated with the incorporation of MWCNT, which acts as a conductive and porous framework, increasing the accessible surface area and facilitating electrolyte penetration. The mesoporous architecture of the composite is expected to promote rapid ion diffusion and efficient charge transport, thereby contributing to the improved electrochemical performance [2].

The morphological features of Bi_2O_3, PCC, MWCNT, and the Bi_2O_3/PCC/MWCNT composite were investigated by FESEM, as presented in Figs. 6, 7, 8 and 9. The Bi_2O_3 sample exhibits plate-like and irregularly shaped particles with a relatively dense and agglomerated structure, indicating the formation of crystalline oxide domains [33]. The PCC sample consists of aggregated micro- and submicron-sized particles, displaying a comparatively compact morphology characteristic of precipitated calcium carbonate. In contrast, the MWCNT sample shows an entangled network of nanotubes, forming a fibrous and highly porous structure. This morphology provides large interstitial voids that are favorable for electrolyte diffusion [34].

The Bi_2O_3/PCC/MWCNT composite exhibits a heterogeneous interconnected morphology in which particulate domains coexist with the entangled nanotubular network. The MWCNTs are distributed throughout and between the particulate domains, forming conductive pathways, while the Bi_2O_3- and PCC-containing particles are integrated within this network. Such morphological integration is expected to facilitate interparticle contact and electrolyte accessibility while maintaining the distinct morphological features of the constituent materials.

To further verify the spatial coexistence and distribution of the constituent elements within the ternary composite, SEM–EDS elemental mapping was performed on the Bi_2O_3/PCC/MWCNT sample. As shown in Fig. 10, elemental maps acquired from the same analyzed region reveal the spatial distribution of C, O, Bi, and Ca. The simultaneous detection and spatial distribution of Bi and O are consistent with the Bi_2O_3-containing domains, whereas the presence of Ca is associated with the PCC component. Carbon is also observed within the investigated region; however, because carbon is intrinsically present in $CaCO_3$, the C map alone cannot be regarded as specific evidence for MWCNT. Therefore, the incorporation of MWCNT is additionally supported by the characteristic entangled nanotubular morphology observed in the FESEM images. Overall, the SEM–EDS mapping results provide direct spatial evidence for the coexistence of the constituent elements within the composite and complement the morphological, structural, and spectroscopic evidence obtained from FESEM, XRD, and FTIR.

For the Bi_2O_3/PCC/MWCNT composite, a heterogeneous and hierarchical morphology is observed, in which Bi_2O_3 and PCC particles are homogeneously distributed within the conductive MWCNT network. The nanotube framework acts as a conductive scaffold that suppresses severe particle agglomeration and promotes the formation of an open and porous architecture. This composite microstructure facilitates electron transport and enhances ion accessibility, thereby contributing to the improved electrochemical performance of the composite electrode [35].

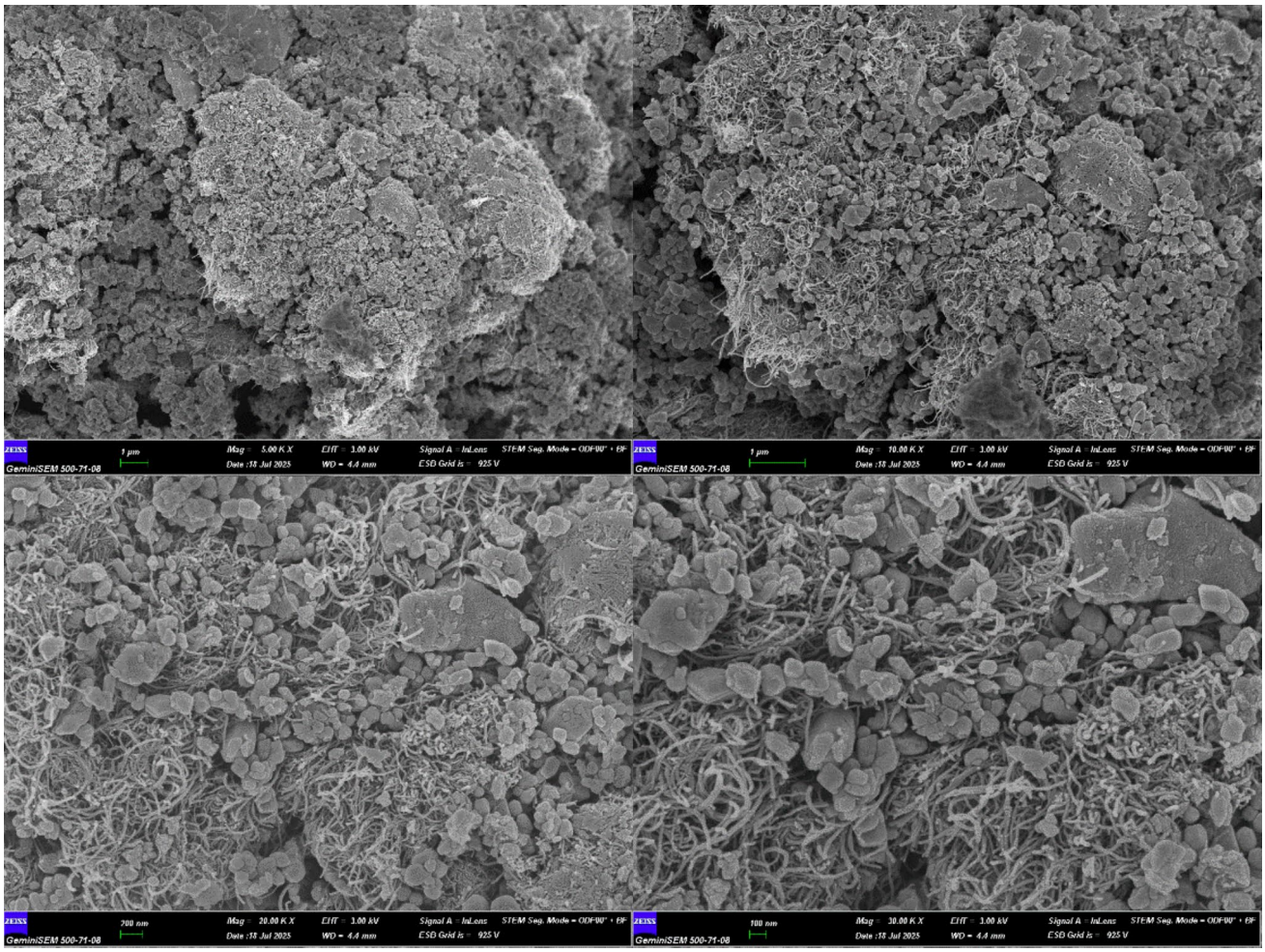

Fig. 6 FESEM images of the Bi_2O_3/PCC/MWCNT composite at different magnifications

In this study, the supercapacitor performance of electrodes based on Bi_2O_3, PCC, MWCNT, and their ternary composite was evaluated within a PVDF/DMF matrix. Electrochemical tests clearly revealed the characteristic behavior of each electrode in terms of specific capacitance, e

nergy and power density, and long-term cycling efficiency [36].

The GCD, CV, and EIS results of the Bi_2O_3/PVDF/DMF electrode are presented in Fig. 11a-c. The GCD curves recorded at different current densities exhibit quasi-triangular profiles, indicating pseudocapacitive behavior associated with Bi–O redox reactions. The decrease in discharge time with increasing current density reflects the limited utilization of active sites under high-rate conditions [37]. The CV curves display distinct redox peaks, confirming the pseudocapacitive nature of the Bi_2O_3/PVDF/DMF electrode. Slight shifts in peak positions with increasing scan rate can be attributed to polarization effects and kinetic limitations. The Nyquist plot shows a small intercept at high frequency corresponding to the solution resistance (Rs), followed by a semicircle related to the charge-transfer resistance (Rct). The inclined line observed in the low-frequency region represents Warburg impedance, indicating ion diffusion limitations and the intrinsically low conductivity of Bi_2O_3/PVDF/DMF [38, 39].

The GCD, CV, and EIS results of the MWCNT/PVDF/DMF electrode are shown in Fig. 11d-f. The GCD curves recorded at different current densities display nearly symmetric triangular shapes, indicating typical electric double-layer capacitive behavior. The gradual decrease in discharge time with increasing current density suggests reduced ion diffusion and limited charge utilization at high rates.

The CV curves obtained at various scan rates exhibit quasi-rectangular shapes with no pronounced redox peaks, confirming that the charge storage mechanism of MWCNT/PVDF/DMF is mainly governed by electrostatic charge accumulation. The increase in current response with increasing scan rate reflects the good rate capability of the nanotube network. The Nyquist plot shows a small intercept in the high-frequency region corresponding to the Rs, followed

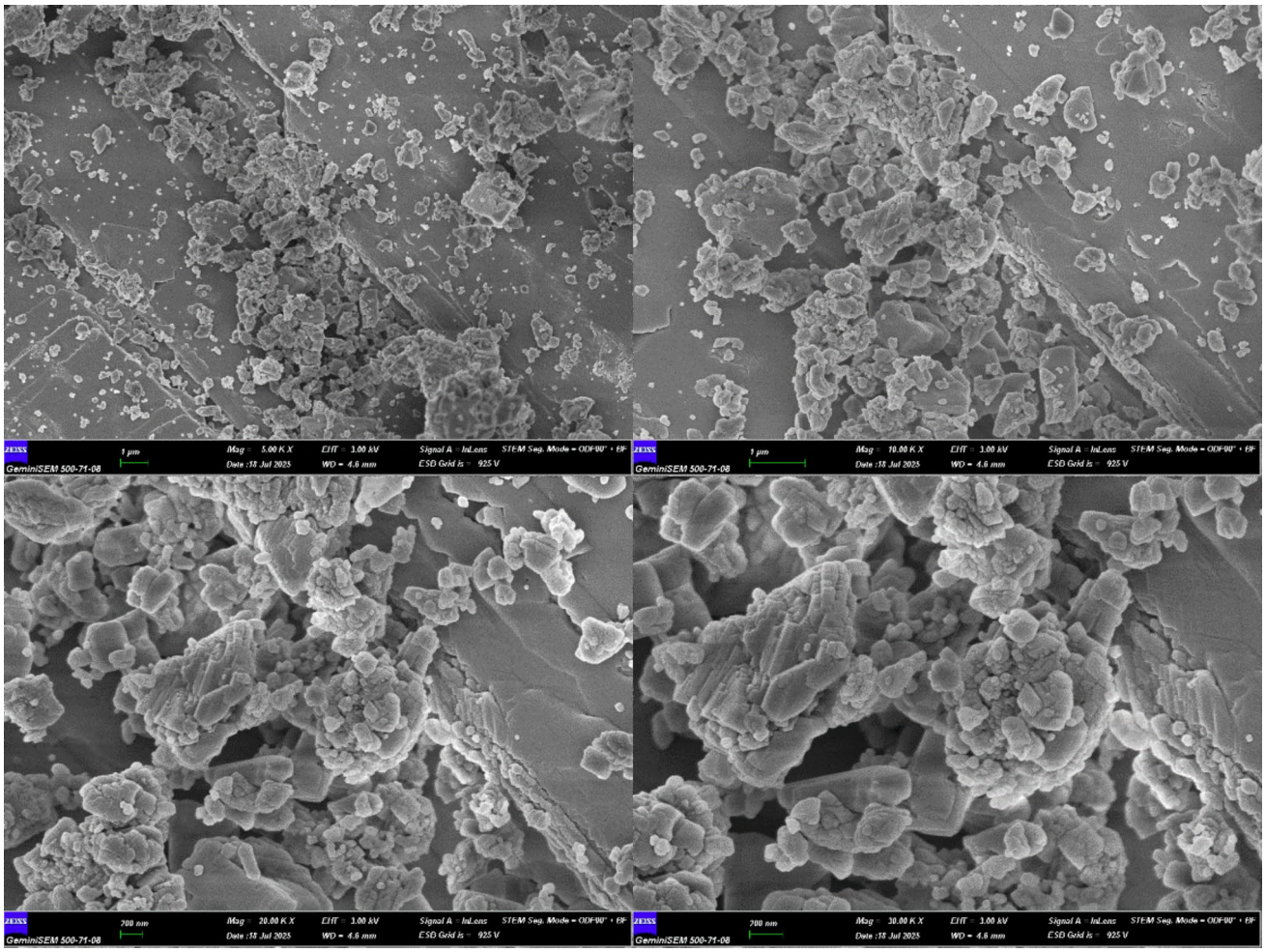

Fig. 7 FESEM images of the PCC at different magnifications

by a small semicircle associated with Rct. The nearly vertical line in the low-frequency region indicates favorable ion diffusion behavior, which can be attributed to the interconnected and conductive nanotube network of MWCNT/PVDF/DMF [39, 40]. To further interpret the charge-transfer and diffusion characteristics of the prepared electrodes, the EIS spectra were fitted using an equivalent circuit model consisting of solution resistance (R_s), charge-transfer resistance (R_ct), a constant phase element (CPE) replacing an ideal capacitor to account for surface heterogeneity, and Warburg impedance (W) reflecting semi-infinite diffusion at low frequencies (Fig. 12). The fitted parameters are summarized in Table 5.

The R_s values of all electrodes are comparable (~0.61–0.82 Ω), indicating similar electrolyte–electrode contact conditions. In contrast, significant differences are observed in R_ct: the MWCNT/PVDF electrode exhibits a relatively low R_ct (~1.23 Ω), consistent with its high electrical conductivity, whereas Bi_2O_3/PVDF shows the highest R_ct (~4.65 Ω), reflecting the intrinsically poor conductivity of the oxide phase. The ternary composite displays a markedly reduced R_ct (~0.87 Ω) compared with Bi_2O_3/PVDF (4.65 Ω) and PCC/PVDF (3.88 Ω), confirming that the incorporation of MWCNT into the composite matrix substantially enhances interfacial charge-transfer kinetics. The Warburg coefficient (σ_w) values further indicate that the composite electrode (0.52 $\Omega \cdot s^{-0} \cdot 5$) offers superior ion diffusion pathways compared to Bi_2O_3/PVDF (2.14 $\Omega \cdot s^{-0} \cdot 5$), PCC/PVDF (1.87 $\Omega \cdot s^{-0} \cdot 5$), and MWCNT/PVDF (0.74 $\Omega \cdot s^{-0} \cdot 5$), in agreement with the BET and FESEM observations. The Nyquist plots of all electrodes were fitted using a single equivalent circuit model, R_s(CPE_dl R_ct)W (Fig. 12), which was found to be appropriate for all four compositions as confirmed by $\chi 2$ values below $10^{-}2$. The fitted parameters are summarized in Table 5.

To further clarify the physical origin of these fitted parameters, the CPE replaces an ideal capacitor in the equivalent circuit to account for the non-ideal, frequency-dispersive capacitive response that arises from surface roughness, porosity, and non-uniform current distribution across

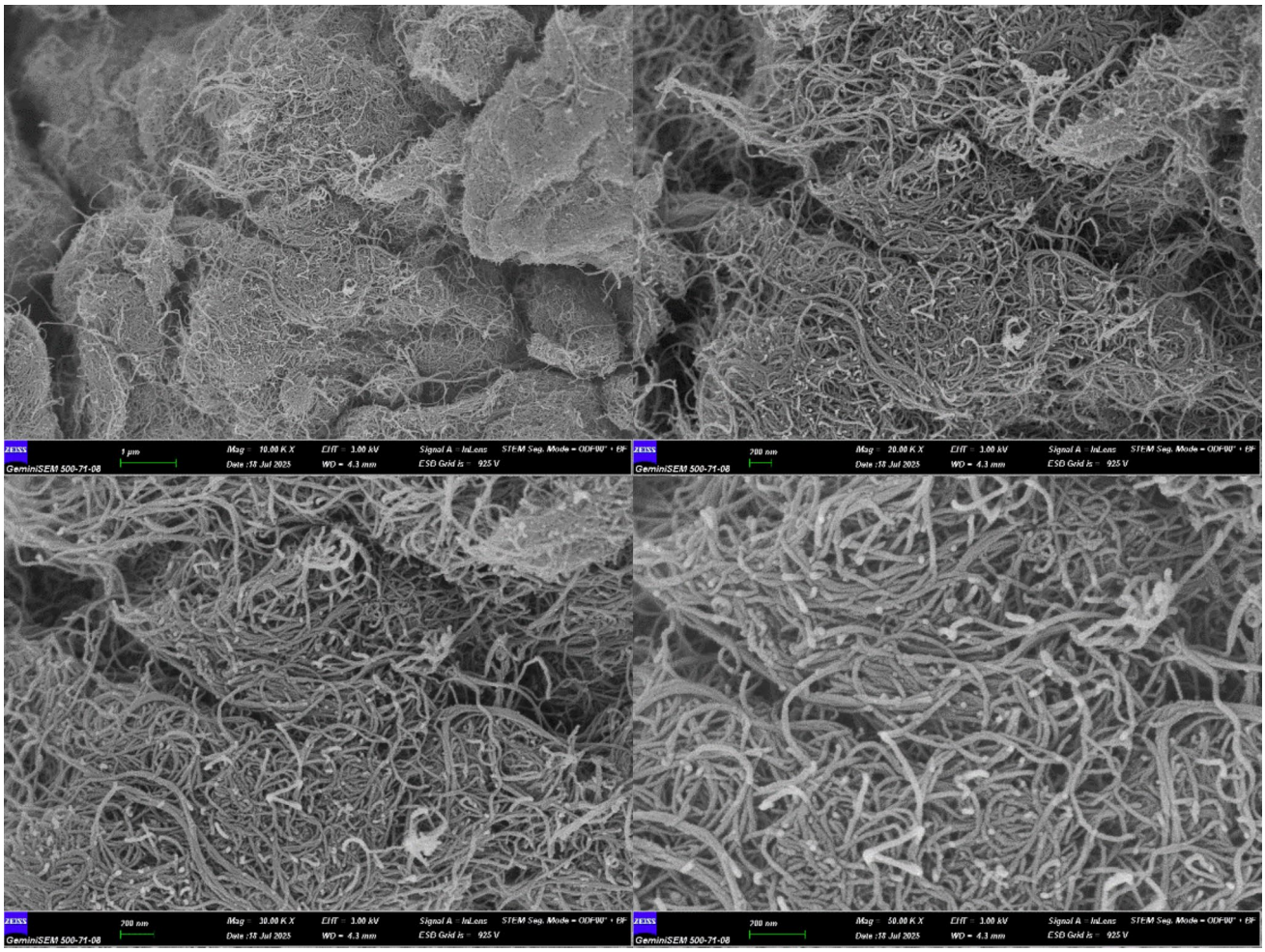

Fig. 8 FESEM images of the MWCNT at different magnifications

a heterogeneous electrode surface. The associated exponent n ($0<n\leq1$) quantifies the deviation from ideal capacitive behavior, with $n=1$ corresponding to a perfect capacitor and lower values indicating greater surface heterogeneity. The increase in n from 0.78 (Bi_2O_3) to 0.82 (PCC) to 0.91 (MWCNT) parallels the FESEM observations, in which pristine Bi_2O_3 displays a dense, agglomerated, irregular morphology (low n), whereas the interconnected MWCNT network behaves closer to an ideal capacitive interface (high n). The composite shows an intermediate-to-high n value (0.88) together with the largest CPE magnitude (CPE-T = 0.0274 $F \cdot s^{n-1}$) among all electrodes; the elevated CPE-T reflects a larger effective double-layer/pseudocapacitive interface, consistent with the distributed Bi_2O_3-containing domains within the MWCNT-containing composite network observed by FESEM and EDS mapping, while the intermediate n value reflects a surface that remains more heterogeneous than the purely carbon-based MWCNT network. The Warburg element, in turn, represents semi-infinite linear diffusion of ions within the porous electrode/electrolyte interface at low frequency, and its coefficient is inversely related to the ion diffusion coefficient and the effective diffusion path length within the electrode. The progressive decrease in the Warburg coefficient from Bi_2O_3 (2.14 $\Omega \cdot s^{-0 \cdot 5}$) to the composite (0.52 $\Omega \cdot s^{-0 \cdot 5}$) therefore reflects a shortened, less tortuous ion diffusion pathway. Notably, the composite exhibits a lower Warburg coefficient than MWCNT alone (0.74 $\Omega \cdot s^{-0 \cdot 5}$) despite its considerably lower surface area, indicating that ion diffusion in this system is governed less by total surface area and more by the accessibility and connectivity of the pore network, within the conductive and porous multicomponent composite network. Taken together, the simultaneous decrease in R_ct, increase in CPE-T, and decrease in the Warburg coefficient for the composite indicate that its improved electrochemical performance stems from three physically distinct but complementary effects: faster interfacial electron transfer enabled by the MWCNT conductive network, a larger effective capacitive interface enabled by homogeneous Bi_2O_3 dispersion, and shorter, less hindered ion diffusion pathways enabled by the mesoporous, PCC-assisted architecture.

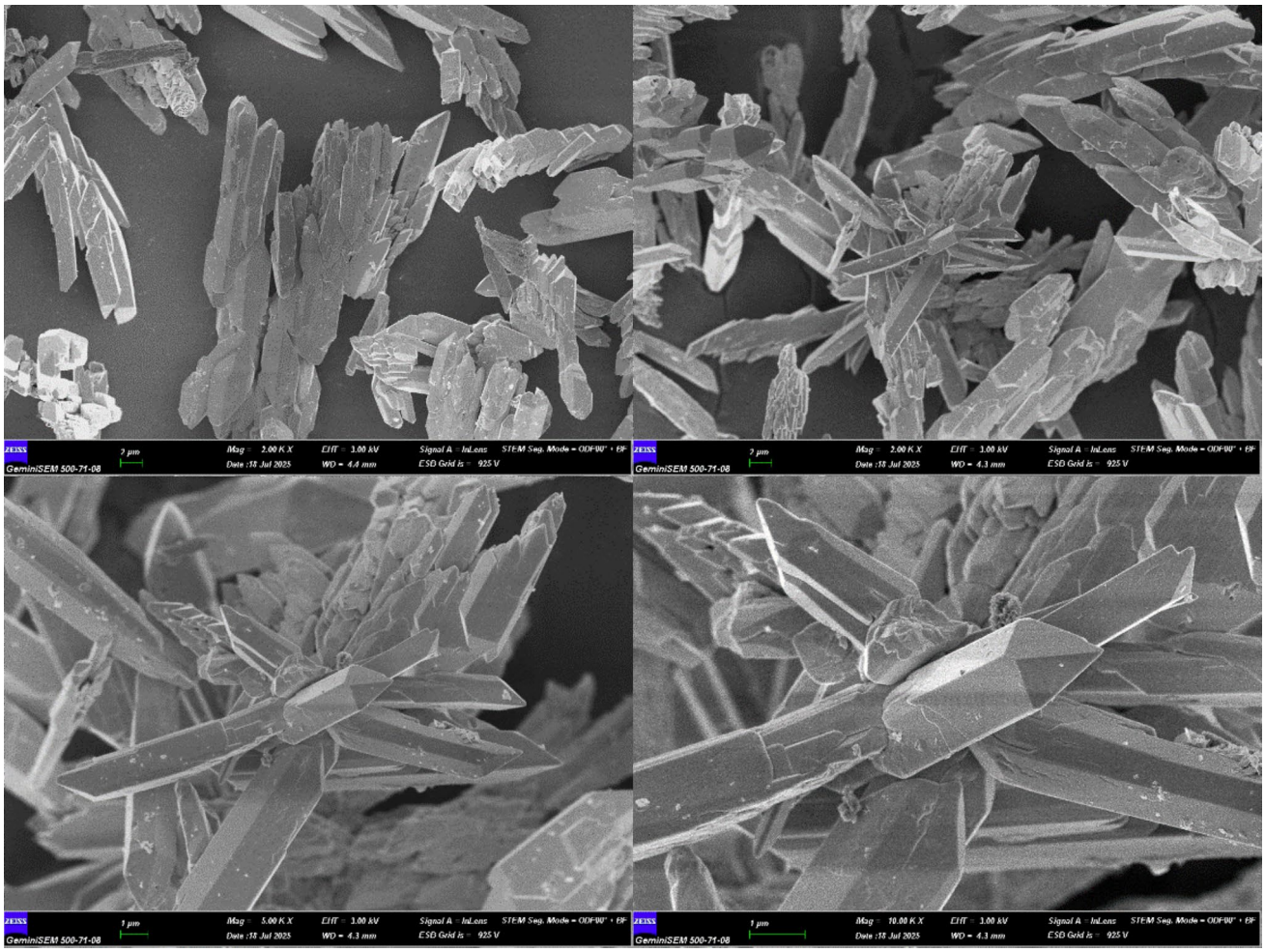

Fig. 9 FESEM images of the Bi_2O_3 at different magnifications

The GCD, CV, and EIS results of the PCC/PVDF/DMF electrode are shown in Fig. 11g-i. The GCD curves obtained at different current densities exhibit quasi-triangular profiles with deviations from ideal linearity, indicating mixed capacitive and faradaic charge storage behavior. The decrease in discharge time with increasing current density reflects limited ion accessibility and slower reaction kinetics at high rates. The CV curves show broad redox features rather than ideal rectangular shapes, suggesting that surface-related faradaic processes contribute to the charge storage mechanism. The current response increases with scan rate, while slight distortions in curve shape are observed due to polarization effects. The Nyquist plot presents a noticeable intercept in the high-frequency region and a depressed semicircle, followed by an inclined line in the low-frequency region. This behavior indicates significant charge-transfer resistance and ion diffusion limitations, consistent with the relatively low electrical conductivity of PCC/PVDF/DMF [41].

The GCD, CV, and EIS results of the composite electrode are presented in Fig. 11j-l. The GCD curves obtained at different current densities exhibit longer discharge times and improved symmetry compared to the single-component electrodes, indicating enhanced charge storage capability and better rate performance [42]. The decrease in discharge time with increasing current density is less pronounced, suggesting more efficient utilization of active sites at high rates. The CV curves show higher current response and broader redox features, reflecting the synergistic contribution of the composite constituents to the charge storage process [43]. The preservation of curve shape with increasing scan rate indicates favorable kinetic behavior and improved ion transport within the electrode structure. The Nyquist plot reveals a reduced semicircle diameter and a steeper low-frequency line compared to the individual electrodes, indicating lower charge-transfer resistance and improved ion diffusion. These features confirm that the composite architecture facilitates faster electron transport and more accessible electrolyte pathways, resulting in superior electrochemical performance [44].

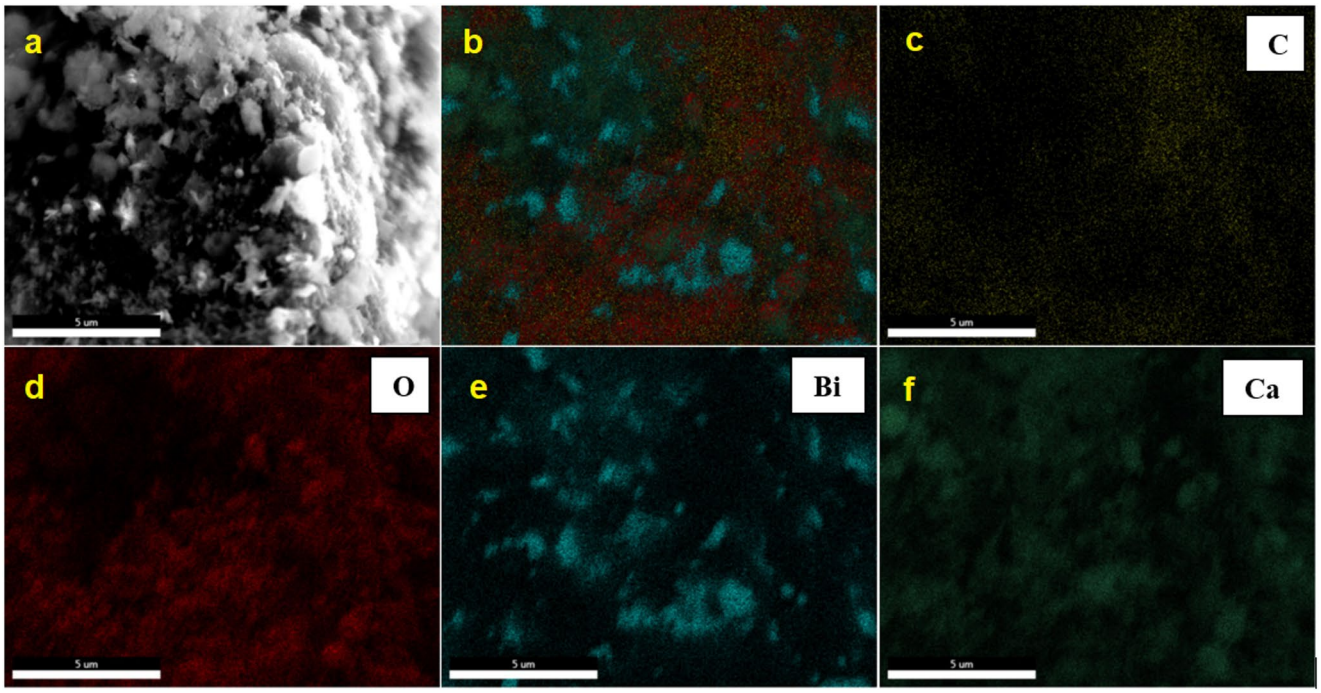

Fig. 10 SEM–EDS elemental mapping of the Bi_2O_3/PCC/MWCNT ternary composite: (**a**) SEM image of the analyzed region, (**b**) elemental overlay, and corresponding elemental distribution maps of (**c**) C, (**d**) O, (**e**) Bi, and (**f**) Ca

The data in Table 6 clearly demonstrate that the Bi_2O_3/MWCNT/PCC/PVDF/DMF composite electrode outperforms the individual components in terms of specific capacitance over the entire range of current densities. Even at a high current density of 10 A g^{-1}, the composite retains 899.6 F g^{-1}, underscoring its excellent rate capability enabled by synergistic charge transport pathways and effective activation of electroactive sites.

As presented in Table 6, the Bi_2O_3/MWCNT/PCC/PVDF/DMF composite electrode delivers the highest energy density over the entire range of current densities. At 1 A g^{-1}, the composite achieves an energy density of 196 Wh kg^{-1}, which exceeds those of Bi_2O_3/PVDF/DMF (147 Wh kg^{-1}), PCC/PVDF/DMF (133 Wh kg^{-1}), and MWCNT/PVDF/DMF (176 Wh kg^{-1}). With increasing current density, a progressive decrease in energy density is observed for all electrodes, which is mainly attributed to reduced charge storage efficiency at high rates.

Nevertheless, the composite electrode preserves superior values, maintaining 127 Wh kg^{-1} at 10 A g^{-1}. This enhanced energy density performance can be ascribed to the synergistic contribution of Bi_2O_3, PCC, and MWCNT within the composite architecture, which promotes more effective ion transport and improved utilization of electroactive sites under high-rate conditions.

As listed in Table 6, the power density of all electrodes increases markedly with increasing current density, reflecting the typical behavior of supercapacitor systems under high-rate operation. At 1 A g^{-1}, the power density values of the electrodes are very close to each other, ranging from 508 to 513 W kg^{-1}, indicating comparable initial power output. With increasing current density, all electrodes exhibit a significant rise in power density, reaching values in the range of 4905–5126 W kg^{-1} at 10 A g^{-1}. The Bi_2O_3/MWCNT/PCC/PVDF/DMF composite electrode maintains power density values comparable to those of the single-component systems over the entire current density range, while simultaneously delivering higher energy density and specific capacitance (Table 6). This combination demonstrates that the composite electrode achieves a favorable balance between energy density and power density, which is essential for practical high-performance energy storage applications.

As presented in Table 7, the cycling stability of the electrodes exhibits pronounced differences depending on their composition. At a current density of 30 A g^{-1}, the MWCNT/PVDF/DMF electrode delivers the highest initial capacitance (346 F g^{-1}), whereas the Bi_2O_3/MWCNT/PCC/PVDF/DMF composite shows a moderate initial value of 278.2 F g^{-1}. However, significant variations are observed in capacitance retention during prolonged cycling. After 10,000 charge–discharge cycles, the composite electrode retains 37% of its initial capacitance, which is markedly higher than that of Bi_2O_3/PVDF/DMF (22.10%) and MWCNT/PVDF/DMF (15%). Although PCC/PVDF/DMF exhibits the highest long-term retention (53%), its initial capacitance is considerably lower than that of the composite and MWCNT-based electrodes. The improved cycling stability

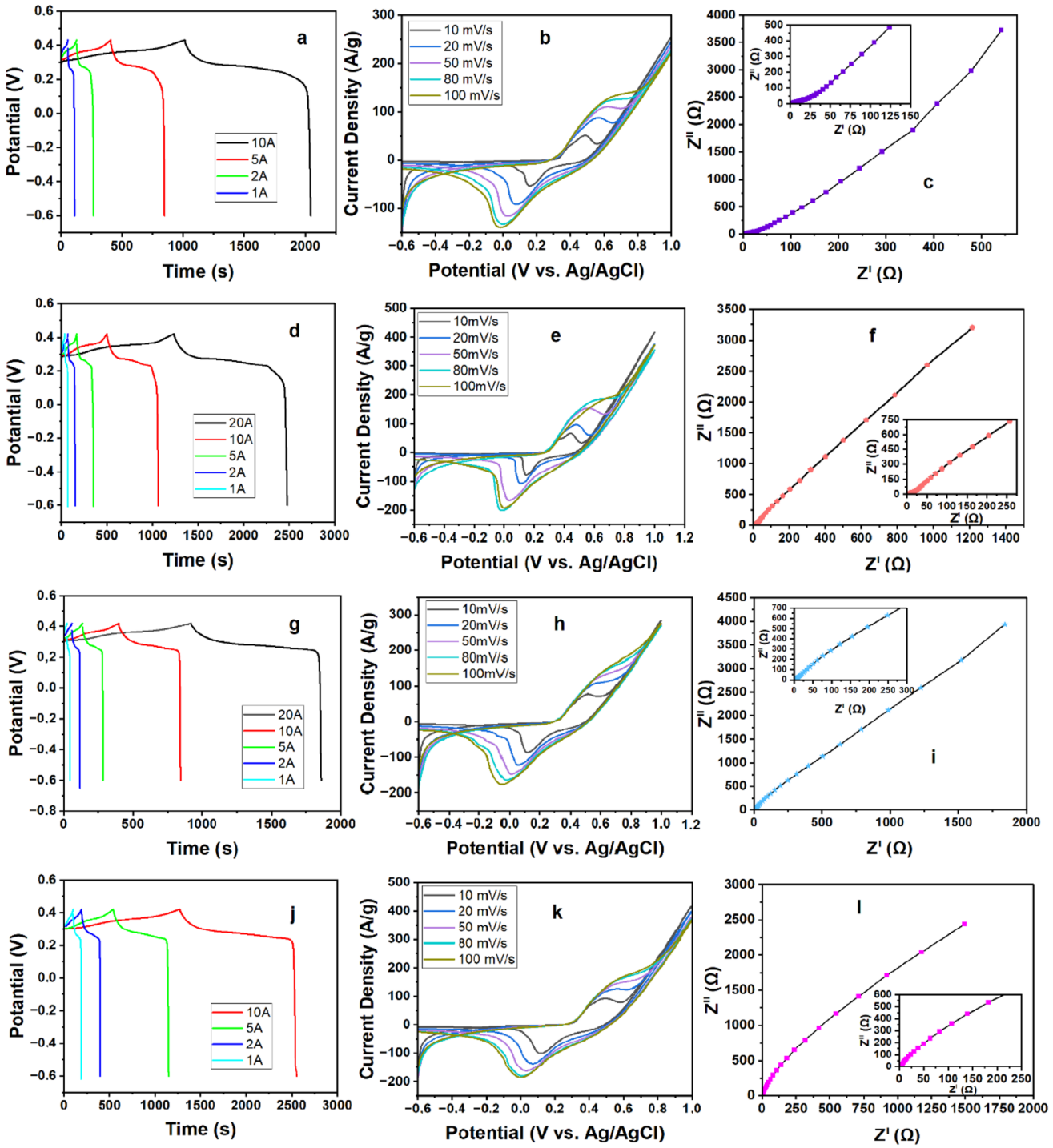

Fig. 11 Electrochemical characterization of electrospinning assisted coating PVDF/DMF electrodes containing (**a**–**c**) 1% Bi_2O_3, (**d**–**f**) 1% MWCNT, (**g**–**i**) 1% PCC, and (**j**–**l**) 1% Bi_2O_3/PCC/MWCNT on nickel foam: galvanostatic charge–discharge (1 A g^{-1}), cyclic voltammetry (100 mV s^{-1}), and EIS Nyquist plots

of the composite electrode compared with the Bi_2O_3 and MWCNT electrodes can be attributed to the stabilizing role of PCC within the composite structure, which likely mitigates structural degradation and preserves electrode integrity during repeated charge–discharge processes.

These results demonstrate that the ternary composite provides a balanced combination of relatively high capacitance and moderately improved cycling durability compared with the Bi_2O_3- and MWCNT-only electrodes; however, its absolute retention (37% after 10,000 cycles) remains below that

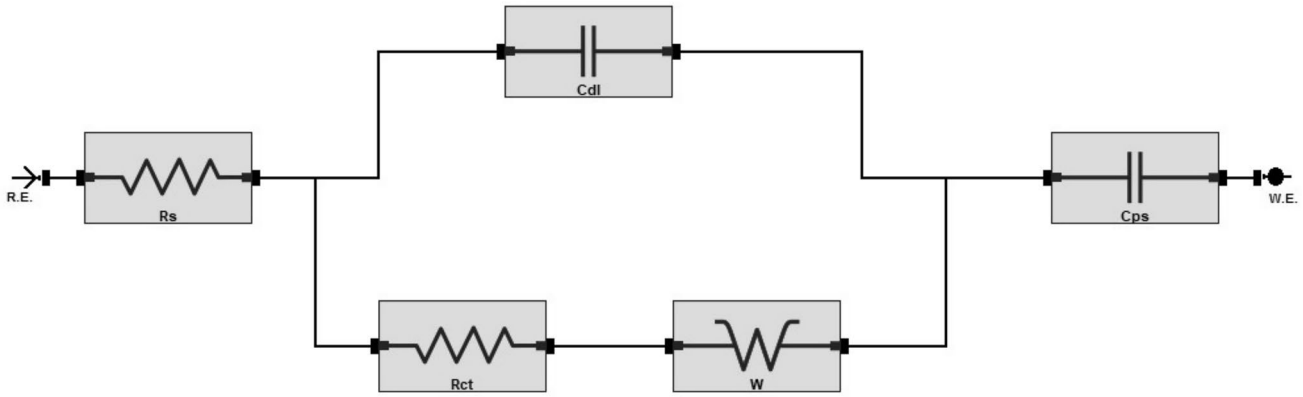

Fig. 12 Equivalent circuit model R_s(CPE_dl R_ct)W used for EIS data fitting of all electrode compositions

Table 5 EIS equivalent circuit parameters

Electrode	R_s (Ω)	R_{ct} (Ω)	CPE-T ($F \cdot s^{n-1}$)	*n*	W ($\Omega \cdot s^{0.5}$)	χ2
Bi_2O_3/PVDF/DMF	0.82	4.65	0.0031	0.78	2.14	3.2×10^{-3}
PCC/PVDF/DMF	0.79	3.88	0.0042	0.82	1.87	2.8×10^{-3}
MWCNT/PVDF/DMF	0.61	1.23	0.0189	0.91	0.74	1.4×10^{-3}
Bi_2O_3/MWCNT/PCC/PVDF/DMF	0.58	0.87	0.0274	0.88	0.52	1.1×10^{-3}

Table 6 Comparative electrochemical performance of the fabricated electrodes in terms of specific capacitance, energy density, and power density at different current densities

Electrode	Current density	Specific capacitance (F g^{-1})	Energy density (Wh kg^{-1})	Power density (W kg^{-1})
Bi_2O_3/PVDF/DMF	1 A	1003	147	513
PCC/PVDF/DMF	1 A	926.4	133	508
MWCNT/PVDF/DMF	1 A	1221.9	176	509
Bi_2O_3/MWCNT/PCC/PVDF/DMF	1 A	1359.5	196	509
Bi_2O_3/PVDF/DMF	2 A	862.75	125	1020
PCC/PVDF/DMF	2 A	878.6	126	1015
MWCNT/PVDF/DMF	2 A	1098.7	159	1020
Bi_2O_3/MWCNT/PCC/PVDF/DMF	2 A	1193.3	171	1017
Bi_2O_3/PVDF/DMF	5 A	684.9	96	2514
PCC/PVDF/DMF	5 A	738.3	102	2492
MWCNT/PVDF/DMF	5 A	909.3	129	2531
Bi_2O_3/MWCNT/PCC/PVDF/DMF	5 A	1004	141	2508
Bi_2O_3/PVDF/DMF	10 A	564.3	75	4905
PCC/PVDF/DMF	10 A	601.9	88	5126
MWCNT/PVDF/DMF	10 A	796.1	109	4965
Bi_2O_3/MWCNT/PCC/PVDF/DMF	10 A	899.6	127	5030

Table 7 Cycling performance and capacitance retention of Bi_2O_3/PVDF/DMF, PCC/PVDF/DMF, MWCNT/PVDF/DMF, and Bi_2O_3/MWCNT/PCC/PVDF/DMF electrodes measured at a current density of 30 A g^{-1} and after 1000, 5000, and 10,000 charge–discharge cycles

Electrode	30 A g^{-1}	1000 cycle	5000 cycle	10000 cycle
Bi_2O_3/PVDF/DMF	87.15 F g^{-1}	51.20%	28.40%	22.10%
PCC/PVDF/DMF	91.3 F g^{-1}	94%	76%	53%
MWCNT/PVDF/DMF	346 F g^{-1}	62%	32%	15%
Bi_2O_3/MWCNT/PCC/PVDF/DMF	278.2 F g^{-1}	63%	42%	37%

of the PCC-only electrode (53%), indicating that further optimization of the composite formulation is needed to fully translate PCC's stabilizing effect into long-term cycling performance [32, 35, 45].

As presented in Table 8, all electrodes exhibit a decrease in specific capacitance when the current density increases from 1 to 10 A g^{-1}, reflecting the typical rate limitation associated with reduced ion diffusion and incomplete utilization of active sites at high current densities. The Bi_2O_3/MWCNT/PCC/PVDF/DMF composite electrode shows the highest capacitance values at both current densities, with

Table 8 Capacitance retention and loss of Bi_2O_3/PVDF/DMF, PCC/PVDF/DMF, MWCNT/PVDF/DMF, and Bi_2O_3/MWCNT/PCC/PVDF/DMF electrodes calculated from specific capacitance values measured at 1 and 10 A g^{-1}

Electrode	C_1 (F g^{-1})	C_{10} (F g^{-1})	Retention (%)	Loss (%)
Bi_2O_3/PVDF/DMF	1003	564.3	56.3	43.7
PCC/PVDF/DMF	926.4	601.9	65.0	35.0
MWCNT/PVDF/DMF	1221.9	796.1	65.2	34.8
Bi_2O_3/MWCNT/PCC/PVDF/DMF	1359.5	899.6	66.2	33.8

$C_1 = 1359.5$ F g^{-1} and $C_{10} = 899.6$ F g^{-1}. Correspondingly, it achieves the highest capacitance retention (66.2%) and the lowest capacitance loss (33.8%) among the investigated electrodes (Table 8).

In comparison, Bi_2O_3/PVDF/DMF exhibits the lowest retention (56.3%) and the highest loss (43.7%), indicating inferior rate capability. PCC/PVDF/DMF and MWCNT/PVDF/DMF show intermediate behavior, with retention values of 65.0% and 65.2%, respectively. The superior retention performance of the composite electrode demonstrates its improved rate capability, which can be attributed to the synergistic effect of Bi_2O_3, PCC, and MWCNT, enabling more efficient charge transport and better accessibility of electroactive sites under high-rate conditions.

The electrochemical performance of Bi_2O_3, PCC, MWCNT, and the Bi_2O_3/PCC/MWCNT composite electrodes was evaluated by galvanostatic charge–discharge measurements at different current densities (Fig. 13). For all electrodes, the specific capacitance decreases with increasing current density, which can be attributed to kinetic limitations and incomplete utilization of electroactive sites at high charge–discharge rates. The Bi_2O_3/PCC/MWCNT composite exhibited the highest specific capacitance among the investigated electrodes, reaching 1359.5 F g^{-1} at 1 A g^{-1}, compared with 1221.9 F g^{-1} for MWCNT, 1003 F g^{-1} for Bi_2O_3, and 926.4 F g^{-1} for PCC. Relative to the best-performing individual component, MWCNT, the ternary composite therefore

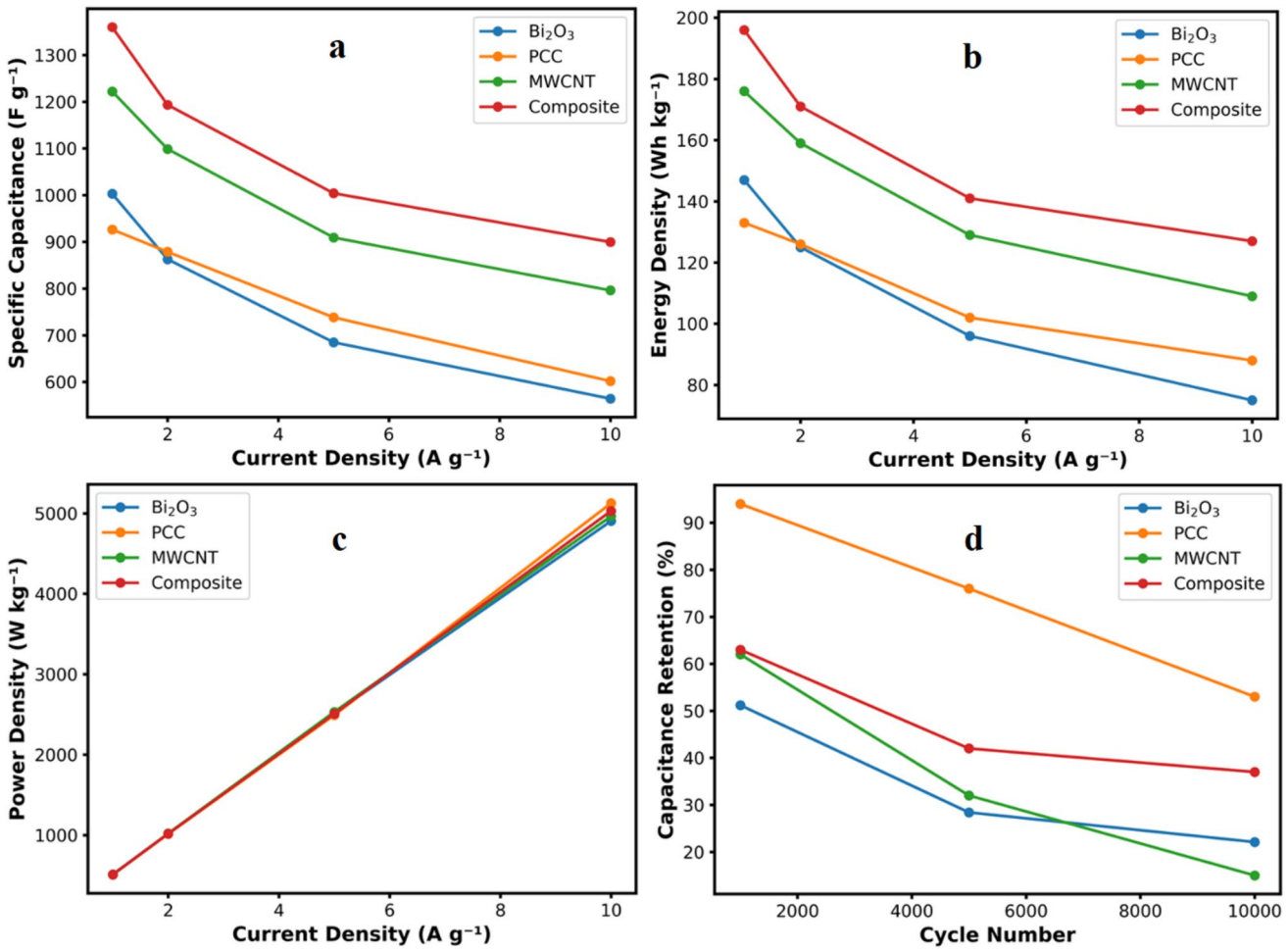

Fig. 13 **a**) Specific capacitance of the electrodes as a function of current density. **b**) Energy density variation of the fabricated electrodes at different current densities. **c**) Power density comparison of electrodes at various current densities. **d**) Cycling stability and capacitance retention of the electrodes up to 10,000 cycles

provides an approximately 11.3% increase in specific capacitance. Although this improvement indicates a beneficial effect of combining the three components, its magnitude does not justify describing the response as a strongly synergistic or non-additive enhancement. Accordingly, the electrochemical improvement is interpreted more cautiously as arising from the complementary contributions of the constituent materials within the composite architecture.

The variation of energy density with current density follows a similar decreasing trend for all electrodes. Despite this decline, the composite electrode maintains higher energy density values compared with the single-component systems, demonstrating its superior charge storage capability. The corresponding power density analysis shows that higher power densities are achieved at elevated current densities for all samples, while the composite preserves a more balanced relationship between energy density and power density. This result suggests that the composite electrode is capable of delivering energy efficiently under high-rate conditions.

Cycling stability results reveal that the composite electrode retains 37% of its initial capacitance after 10,000 charge–discharge cycles, which is higher than the values obtained for the Bi_2O_3 (22.1%) and MWCNT (15%) electrodes. This improvement can be associated with the stabilizing effect of PCC, which likely mitigates structural degradation during prolonged cycling. It should be emphasized, however, that a 37% retention still represents a substantial loss of capacitance over extended cycling and remains below the retention achieved by the PCC-only electrode (53%), indicating that long-term durability is a limitation of the present composite that warrants further optimization rather than a fully resolved feature of the design.

The Ragone plot further confirms that the composite electrode maintains a favorable balance between energy density and power density across the operational range. In comparison with the single-component electrodes, the composite achieves relatively higher energy densities at comparable power densities, highlighting its improved energy–power trade-off (Fig. 14).

A trend-based statistical analysis was conducted to quantitatively assess the rate capability of the electrodes. The capacitance retention values, calculated using the relation Retention (%) = $(C_{10}/C_1) \times 100$, show that the composite electrode preserves 66.2% of its initial capacitance when the current density increases from 1 to 10 A g^{-1}. This value is higher than those of Bi_2O_3 (56.3%), PCC (65.0%), and MWCNT (65.2%). In addition, a strong linear correlation ($R^2 \approx 0.99$) is observed between specific capacitance and energy density for all electrodes, indicating that the energy storage behavior is primarily governed by capacitance variation.

The enhanced electrochemical performance of the Bi_2O_3/PCC/MWCNT composite electrode arises from the complementary contributions of pseudocapacitive Bi_2O_3, the conductive pathways formed by MWCNT, and the structural stabilization provided by PCC. These complementary contributions are directly supported by the EIS-fitted parameters in Table 5: the charge-transfer resistance of the composite (Rct = 0.87 Ω) is lower not only than that of Bi_2O_3 (4.65 Ω) and PCC (3.88 Ω), but also than that of MWCNT alone (1.23 Ω), while the Warburg coefficient of the composite (0.52 $\Omega \cdot s^{-0.5}$) is likewise the lowest among all electrodes. These values indicate that the combination of the three components contributes to improved charge-transfer and ion-diffusion behavior within the composite electrode. This interpretation is further corroborated by the BET and FESEM results, which show that the composite retains an intermediate, accessible mesoporous architecture (SBET = 71.21 m^2 g^{-1}) in which Bi_2O_3-containing domains are distributed within the MWCNT-containing network in the presence of PCC, rather than the pore-blocking or agglomerated morphology observed for pristine Bi_2O_3. Consistent with this structural and kinetic evidence, the composite's specific capacitance (1359.5 F g^{-1}) exceeds the values obtained for any individual component, indicating a beneficial effect of combining the three components on charge storage performance. Consequently, the composite also exhibits improved rate capability and moderately enhanced cycling stability relative to the individual Bi_2O_3 and MWCNT electrodes, although its cycling retention remains lower than that of the PCC electrode. It should be noted, however, that the composite's capacitance retention (37% after 10,000 cycles) remains below that of the PCC-only electrode (53%), indicating that the stabilizing contribution of PCC is only partially retained within the ternary architecture and that the overall cycling durability, while improved, is still limited in absolute terms.

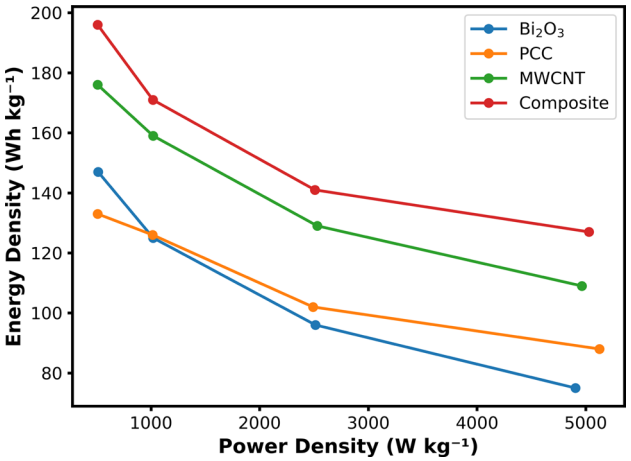

Fig. 14 Ragone plot showing the relationship between energy density and power density

The Ragone plot (Fig. 14) reveals that the ternary composite achieves a maximum energy density of *196 Wh* kg^{-1} at a power density of *509 W* kg^{-1}, outperforming Bi_2O_3/PVDF

(147 Wh kg^{-1}), PCC/PVDF (133 Wh kg^{-1}), and MWCNT/PVDF (176 Wh kg^{-1}) at comparable power densities. Even at an elevated power density of 5030 W kg^{-1}, the composite retains an energy density of 127 Wh kg^{-1}, demonstrating a favorable energy–power trade-off suitable for high-rate supercapacitor applications.

Performance of individual components

The Bi_2O_3-based electrode exhibited a specific capacitance of 1003 F g^{-1} at 1 A g^{-1}, attributable to the faradaic charge storage mechanism associated with Bi^{3+}/Bi^0 redox transitions. However, with increasing current density, the capacitance declined markedly, reaching 564.3 F g^{-1} at 10 A g^{-1}. This reduction is primarily due to the inherently low electrical conductivity of Bi_2O_3, which impedes efficient ion diffusion to the electrode surface. Although the energy density reached 147 Wh kg^{-1} and the power density 513 W kg^{-1} at 1 A g^{-1}, cycling stability was considerably poor. Only 22.1% of the capacitance was retained after 10,000 cycles, indicating that the material is unsuitable for long-term energy storage applications.

The PCC-based electrode, while exhibiting a relatively lower initial specific capacitance of 926.4 F g^{-1}, demonstrated the highest long-term cycling stability among all samples. Notably, it retained 53% of its initial capacitance after 10,000 cycles. Furthermore, it maintained 91.3 F g^{-1} even at a high current density of 30 A g^{-1}, reflecting its structural robustness and consistent charge storage behavior. These findings suggest that PCC serves as a crucial mechanical support phase, preserving electrode integrity and minimizing the loss of active material throughout extended cycling.

The MWCNT-based electrode delivered a high specific capacitance of 1221.9 F g^{-1} and an energy density of 176 Wh kg^{-1} at 1 A g^{-1}, with a corresponding power density of 509 W kg^{-1}. This excellent performance is attributed to the high surface area and outstanding electrical conductivity of MWCNTs, which facilitate rapid electron transfer and efficient double-layer charge accumulation. However, this electrode showed poor cycling stability, with capacitance retention decreasing to 15% after 10,000 cycles. This rapid degradation suggests structural deterioration or unfavorable interactions between the MWCNTs and the electrolyte during prolonged cycling.

Performance of the ternary composite electrode

The Bi_2O_3/MWCNT/PCC ternary composite electrode exhibited the most favorable and balanced electrochemical behavior. It achieved the highest specific capacitance of 1359.5 F g^{-1} at 1 A g^{-1} and maintained 899.6 F g^{-1} at 10 A g^{-1}, surpassing the performance of all individual components. Additionally, it exhibited a high energy density of 196 Wh kg^{-1} and a power density of 509 W kg^{-1}. Regarding cycling stability, the composite retained 63%, 42%, and 37% of its initial capacitance after 1000, 5000, and 10,000 cycles, respectively. While this progressive capacitance loss indicates that the composite still faces notable degradation over extended cycling, the retention obtained after 10,000 cycles nonetheless exceeds that of the Bi_2O_3- and MWCNT-only electrodes, pointing to a partial, rather than complete, resolution of the long-term stability limitation.

The enhanced performance can be attributed to the complementary contributions of the individual components; Bi_2O_3 contributes pseudocapacitance through redox activity, MWCNTs enhance electrical conductivity and facilitate charge transfer, and PCC provides mechanical reinforcement and structural stability. This division of roles is supported by the data presented above: the reduced Rct and Warburg coefficient of the composite support the conductivity/charge-transfer contribution of MWCNT within the redox-active Bi_2O_3 matrix, while the BET/FESEM results support the porosity- and dispersion-related role of PCC. The higher specific capacitance of the composite (1359.5 F g^{-1}) compared with the individual electrodes further indicates the beneficial effect of combining the three components. These complementary contributions enable the composite to maintain favorable electrochemical performance under high current conditions. The balance of redox behavior, conductivity, and mechanical stability highlights the potential of this ternary system for supercapacitor applications.

To further evaluate the significance of the present study, the electrochemical performance of the Bi_2O_3/PCC/MWCNT electrode was compared with representative Bi_2O_3-based composite electrodes reported in recent literature, as summarized in Table 9. The present ternary electrode delivered a high specific capacitance of 1359.5 F g^{-1} at 1 A g^{-1}, which is superior to that of many previously reported Bi_2O_3-based composite electrodes. This enhanced capacitive behavior is attributed to the complementary contributions of the pseudocapacitive Bi_2O_3 phase, the highly conductive MWCNT network, and the mechanically reinforcing PCC framework, which collectively improve charge storage, electron transport, and ion diffusion. Nevertheless, although the initial electrochemical performance is highly competitive, the capacitance retention after 10,000 cycles (37%) remains lower than that reported for several optimized Bi_2O_3/carbon- and Bi_2O_3/polymer-based systems. Therefore, the principal contribution of the present work lies in the improvement in the initial electrochemical performance achieved through the rational design of the ternary architecture, while further optimization of the electrode composition and structural stability is still required to improve long-term cycling durability.

Table 9 Comparison of the electrochemical performance of representative Bi_2O_3-based composite electrodes reported in the literature

Electrode material	Electrolyte/condition	Specific capacitance	Cycling retention	Ref.
Bi_2O_3–MWCNT	6.0 M KOH, 1 A g^{-1}	473 F g^{-1}	88.7% after 3000 cycles	[46]
Bi_2O_3–GO	1 A g^{-1}	1029 F g^{-1}	80% after 3000 cycles	[47]
Bi_2O_3/N-HPC	6 M KOH, 0.5 A g^{-1}	684.9 F g^{-1}	85.2% after 10,000 cycles	[48]
α-Bi_2O_3@rGO	1 A g^{-1}	1144 F g^{-1}	91.71% rate retention at 20 A g^{-1}*	[49]
Defect-rich Bi_2O_3–rGO	1 A g^{-1}	1053 F g^{-1}	84.2% after 1000 cycles	[50]
Bi_2O_3/PANI	1 M Na_2SO_4, 2 A g^{-1}	1447 F g^{-1}	80% after 10,000 cycles	[51]
Bi_2O_3/PCC/MWCNT (this work)	2 M KOH, three-electrode, 1 A g^{-1}	1359.5 F g^{-1}	37% after 10,000 cycles	-

Conclusion

A ternary Bi_2O_3/PCC/MWCNT composite electrode was successfully fabricated via electrospinning assisted coating on nickel foam using a PVDF/DMF matrix for supercapacitor applications. Structural and spectroscopic analyses verified the stable coexistence of α-Bi_2O_3, calcite PCC, and graphitic MWCNT without phase transformation, while BET and FESEM investigations revealed the formation of a highly interconnected mesoporous architecture enabling efficient electrolyte penetration and rapid charge transport.

In a three-electrode half-cell configuration, the composite electrode exhibited a high specific capacitance of 1359.5 F g^{-1} at 1 A g^{-1}, maintaining 899.6 F g^{-1} at 10 A g^{-1}, together with an energy density of 196 Wh kg^{-1}, indicating strong rate capability under increasing current density. Reduced charge-transfer resistance and facilitated ion diffusion behavior were observed compared with single-component electrodes. Long-term cycling measurements confirmed partially improved electrochemical stability relative to the individual Bi_2O_3 and MWCNT electrodes, with the composite retaining 37% of its initial capacitance after 10,000 cycles. This behavior arises from the cooperative interaction between pseudocapacitive Bi_2O_3, conductive MWCNT pathways, and the structural buffering effect of PCC, which partially mitigates degradation during repeated cycling. Nevertheless, this retention level remains below that of the PCC-only electrode (53%) and below the retention typically reported for state-of-the-art supercapacitor electrodes, indicating that long-term cycling durability remains a limitation of the present composite and a priority for further optimization, for example through adjustment of the PCC-to-Bi_2O_3/MWCNT ratio or additional interfacial engineering.

Notably, this work distinguishes itself from previously reported binary Bi_2O_3/carbon nanotube electrodes by identifying and exploiting a distinct structural role for PCC. While MWCNT alone provided the highest initial capacitance (1221.9 F g^{-1} at 1 A g^{-1}) but suffered rapid capacity fading (only 15% retention after 10,000 cycles), and Bi_2O_3 alone exhibited even poorer durability (22.1% retention), the incorporation of PCC as a mechanical buffering phase rather than as a conductive or redox-active component enabled the ternary composite to retain 37% of its capacitance after 10,000 cycles while still delivering the highest overall specific capacitance (1359.5 F g^{-1}) among all tested electrodes. This finding demonstrates that PCC's primary contribution lies in structural reinforcement and stabilization rather than in charge storage or electron transport, offering a design principle that is largely unexplored in conventional Bi_2O_3/CNT-based supercapacitor electrodes.

It should be noted that the electrochemical performance reported herein was obtained under a three-electrode half-cell configuration, and the resulting specific capacitance and energy density values, while indicative of the intrinsic redox and charge-storage capability of the composite material, do not directly represent the performance of a packaged, practical energy storage device. Future work will focus on evaluating the composite electrode in a two-electrode full-cell (symmetric or asymmetric) configuration to assess its viability for real-world supercapacitor applications.

The present electrode design highlights an effective materials engineering strategy in which conductive networks and mechanically stabilizing phases are integrated with redox-active materials to simultaneously improve capacitance, rate performance, and, to a more limited extent, operational stability. Such a multi-component architecture provides a promising platform for the development of high-energy supercapacitor systems, although further improvements in long-term cycling durability will be necessary before these materials can be considered for practical, extended-use applications.

Acknowledgements This research includes a part of the doctoral dissertation conducted by İnci Ünlü under the supervision of Assoc. Prof. Dr. Fatma Kılıç Dokan and Dr. Rifat Battaloğlu.

Author contributions Inci Unlu: Conceptualization, Methodology, Investigation, Formal analysis, Data curation, Visualization, Writing – original draft.
Fatma Kilic Dokan: Methodology, Validation, Formal analysis, Writing – review & editing.

Rifat Battaloglu: Conceptualization, Supervision, Project administration, Resources, Validation, Writing – review & editing.
Ertugrul Sahmetlioglu: Formal analysis, Validation, Writing – review & editing.
All authors have read and approved the final version of the manuscript and agree to be accountable for all aspects of the work, ensuring that questions related to the accuracy or integrity of any part of the work are appropriately investigated and resolved.

Funding This research has been funded by Scientific Research Projects Unit of Niğde Ömer Halisdemir University with project number FMT 2023/6-LÜTEP.

Data availability The datasets generated and analyzed during the current study are available from the corresponding author on reasonable request.

Declarations

Competing interests The authors declare no competing interests.

References

1. Conway BE (1999) Electrochemical supercapacitors: scientific fundamentals and technological applications. Springer
2. Simon P, Gogotsi Y (2008) Materials for electrochemical capacitors. Nat Mater 7(11):845–854. https://doi.org/10.1038/nmat2297
3. Miller JR, Simon P (2008) Electrochemical capacitors for energy management. Science 321(5889):651–652. https://doi.org/10.1126/science.1158736
4. Zhai Y, Dou Y, Zhao D, Fulvio PF, Mayes RT, Dai S (2011) Carbon materials for chemical capacitive energy storage. Adv Mater 23(42):4828–4850
5. Yu A, Roes I, Davies A, Chen Z (2015) Ultrathin, transparent, and flexible supercapacitors based on graphene films. Nano Lett 11(11):4438–4442. https://doi.org/10.1021/nl202650d
6. Zhang L, Zhao X, Wang G (2019) Recent advances in PVDF-based composite electrodes for supercapacitors. Electrochim Acta 296:927–944
7. Wu J, Wang Y, Qiao Y, Wang X (2021) PVDF-based polymer composites for electrochemical energy storage: a review. Prog Polym Sci 118:101405. https://doi.org/10.1016/j.progpolymsci.2021.101405
8. Zhao X, Zhang L, Shi W (2020) PVDF-based flexible solid-state supercapacitors: from material design to device applications. J Mater Chem A 8(21):10676–10694
9. Yuan C, Li Y, Hou L, Zhang X, Shen L, Lou XW (2012) Ultrathin mesoporous $NiCo_2O_4$ nanosheets supported on Ni foam as advanced electrodes for supercapacitors. Adv Funct Mater 22(21):4592–4600
10. An L, Zhang Y, Zhu Y, Zhang H, Wang Y (2020) Facile synthesis of Bi_2O_3/MWCNT nanocomposite for supercapacitor applications. J Alloy Compd 820:153118. https://doi.org/10.1016/j.jallcom.2019.153118
11. Li Y, Wang Y, Wang D, Wu M (2021) Bismuth oxide-based materials for energy storage and conversion: a review. J Mater Chem A 9(12):7266–7290. https://doi.org/10.1039/D0TA11394E
12. Zhang H et al (2020) Bismuth oxide nanostructures for electrochemical energy storage and conversion: a review. Nano Energy 78:105365
13. Rani J, Rana RK, Yadav RM (2020) Hybrid nanostructures of carbon nanotubes and metal oxides for energy storage devices. Nano Energy 75:104962
14. Kaempgen M, Chan CK, Ma J, Cui Y, Gruner G (2009) Printable thin film supercapacitors using single-walled carbon nanotubes. Nano Lett 9(5):1872–1876
15. El-Kady MF, Shao Y, Kaner RB (2016) Graphene for energy storage devices. Nat Rev Mater 1:16033
16. Kumar A, Kumar D, Prasad K (2018) Precipitated calcium carbonate-based nanocomposites for enhanced electrochemical performance. Mater Chem Phys 204:329–336. https://doi.org/10.1016/j.matchemphys.2017.10.039
17. Dong L, Ma Y, Zhang Q, Lu Y (2021) Functional role of $CaCO_3$ nanoparticles in porous composite electrodes. Mater Sci Semicond Process 123:105527
18. Harwig HA (1978) On the structure of bismuth sesquioxide: the α-phase. Mater Res Bull 13(2):119–126. https://doi.org/10.1016/0025-5408(78)90005-3
19. Abu-Dief AM, Mohamed IMA (2017) A review on versatile applications of bismuth oxide (Bi_2O_3) nanostructures: synthesis, characterization, and photocatalytic activity. Mater Res Express 4(3):035039. https://doi.org/10.1088/2053-1591/aa5a3d
20. Antao SM, Hassan I (2007) The orthorhombic structure of calcite, $CaCO_3$, at high pressure. Am Mineral 92(7):1109–1117. https://doi.org/10.2138/am.2007.2514
21. Dresselhaus MS, Dresselhaus G, Saito R, Jorio A (2005) Raman spectroscopy of carbon nanotubes. Phys Rep 409(2):47–99. https://doi.org/10.1016/j.physrep.2005.03.006
22. Kharisov BI, Dias HVR, Kharissova OV, Pérez BO, Pérez VMJ (2014) Bismuth oxide nanostructures: synthesis, characterization and applications. RSC Adv 4(9):4535–4549. https://doi.org/10.1039/C3RA45009A
23. Gunasekaran S, Anbalagan G, Pandi S (2006) Raman and infrared spectra of carbonates of calcite structure. J Raman Spectrosc 37(9):892–899. https://doi.org/10.1002/jrs.1517
24. Vaisman L, Wagner HD, Marom G (2006) The role of surfactants in dispersion of carbon nanotubes. Adv Colloid Interface Sci 128–130:37–46. https://doi.org/10.1016/j.cis.2006.11.007
25. Monthioux M, Kuznetsov VL (2006) Who should be given the credit for the discovery of carbon nanotubes? Carbon 44(9):1621–1623. https://doi.org/10.1016/j.carbon.2006.03.019
26. Hayat HP, Dokan FK, Onses MS, Yılmaz E, Duran A, Sahmetlioglu E (2024) Flexible electrodes composed of flower-like MoS2 and MXene for supercapacitor applications. Mater Res Bull 175:112747
27. Hasan MM, Sadeque MSB, Albasar I, Pecenek H, Dokan FK, Onses MS, Ordu M (2023) Scalable fabrication of MXene-PVDF nanocomposite triboelectric fibers via thermal drawing. Small 19(6):2206107
28. Peçenek H, Yetiman S, Dokan FK, Onses MS, Yılmaz E, Sahmetlioglu E (2022) Effects of carbon nanomaterials and MXene addition on the performance of nitrogen doped MnO2 based supercapacitors. Ceram Int 48(5):7253–7260
29. Singh K, Arora S (2011) Removal of synthetic textile dyes from wastewaters: a critical review on present treatment technologies. Crit Rev Environ Sci Technol 41(9):807–878
30. Sing KSW, Everett DH, Haul RAW, Moscou L, Pierotti RA, Rouquérol J, Siemieniewska T (1985) Reporting physisorption data for gas/solid systems with special reference to the determination of surface area and porosity. Pure Appl Chem 57(4):603–619. https://doi.org/10.1351/pac198557040603
31. Iijima S (1991) Helical microtubules of graphitic carbon. Nature 354(6348):56–58. https://doi.org/10.1038/354056a0
32. Zhang LL, Zhao X (2009) Carbon-based materials as supercapacitor electrodes. Chem Soc Rev 38(9):2520–2531. https://doi.org/10.1039/B813846J
33. Patil SB, Lokhande CD, Kim JH (2017) Bi_2O_3 nanostructures for electrochemical energy storage applications. J Alloy Compd 694:1048–1056. https://doi.org/10.1016/j.jallcom.2016.10.083

34. De Volder MFL, Tawfick SH, Baughman RH, Hart AJ (2013) Carbon nanotubes: present and future commercial applications. Science 339(6119):535–539. https://doi.org/10.1126/science.1222453
35. Wang K, Wu H, Meng Y, Wei Z (2014) Conducting polymer nanowire arrays for high performance supercapacitors. Small 10(1):14–31. https://doi.org/10.1002/smll.201302407
36. Conway BE (1999) Electrochemical supercapacitors: scientific fundamentals and technological applications. Springer. https://doi.org/10.1007/978-1-4757-3058-6
37. Lokhande CD, Dubal DP, Joo OS (2011) Metal oxide thin film based supercapacitors. Curr Appl Phys 11(3):255–270. https://doi.org/10.1016/j.cap.2010.12.001
38. Barsoukov E, Macdonald JR (2005) Impedance spectroscopy: theory, experiment, and applications, 2nd ed. Wiley. https://doi.org/10.1002/0471716243
39. Unlu I, Dokan FK, Battaloglu R et al (2026) Comparative investigation of supercapacitor performance in DMF/PVDF blends: electrospinning-assisted coating, spray coating, and slurry deposition techniques. Chem Pap. https://doi.org/10.1007/s11696-026-04651-6
40. Peçenek H, Dokan FK, Onses MS, Yılmaz E, Sahmetlioglu E (2022) Highly compressible binder-free sponge supercapacitor electrode based on flower-like NiO/MnO2/CNT. J Alloys Compd 913:165053
41. Wang H, Yi H, Chen X, Wang X (2014) Asymmetric supercapacitors based on nano-structured $CaCO_3$ for high performance energy storage. Electrochim Acta 132:67–73. https://doi.org/10.1016/j.electacta.2014.03.148
42. Zhang LL, Zhou R, Zhao XS (2010) Graphene-based materials as supercapacitor electrodes. J Mater Chem 20(29):5983–5992. https://doi.org/10.1039/C000417K
43. Yu G, Hu L, Vosgueritchian M, Wang H, Xie X, McDonough JR, Cui X, Cui Y, Bao Z (2011) Solution-processed graphene/MnO_2 nanostructured textiles for high-performance electrochemical capacitors. Nano Lett 11(7):2905–2911. https://doi.org/10.1021/nl2013828
44. Augustyn V, Simon P, Dunn B (2014) Pseudocapacitive oxide materials for high-rate electrochemical energy storage. Energy Environ Sci 7(5):1597–1614. https://doi.org/10.1039/C3EE44164D
45. Yu G, Xie X, Pan L, Bao Z, Cui Y (2013) Hybrid nanostructured materials for high-performance electrochemical capacitors. Nano Energy 2(2):213–234. https://doi.org/10.1016/j.nanoen.2012.10.010
46. Zhang D, Xiang Q (2022) Electrophoretic co-deposition of Bi_2O_3–multiwalled carbon nanotubes coating as supercapacitor electrode. J Am Ceram Soc 105:5638–5648. https://doi.org/10.1111/jace.18556
47. Hounkanrin SE, Guo Z, Luo J (2023) Microwave-synthesized bismuth oxide-graphene oxide composite as an electrode for supercapacitors. Int J Electrochem Sci 18(4):100086. https://doi.org/10.1016/j.ijoes.2023.100086
48. Zhu W, Shen D (2024) Synthesis of Bi_2O_3/hierarchical porous carbon composites for supercapacitor application. J Energy Storage 79:110118. https://doi.org/10.1016/j.est.2023.110118
49. Yao P, Wang T, Yu H, Li Z, Cheng C, Zhu J (2024) Bi_2O_3@ reduced graphene oxide and $NiCo_2$@ Ni_3Co electrodes for all-electrodeposited high-performance supercapacitors. J Power Sources 613:234958. https://doi.org/10.1016/j.jpowsour.2024.234958
50. Wang T, Cheng C, Guan Z, Tao T, Xiao Q, Zhu J (2025) Chemical reduction-induced defect-rich bismuth oxide-reduced graphene oxide anode for high-performance supercapacitors. J Colloid Interface Sci 677:45–54. https://doi.org/10.1016/j.jcis.2024.07.213
51. Shinde PV, Dutta DP, Chaskar MG, Mane RS (2024) High-performance aqueous supercapacitors with bismuth oxide/polyaniline composite electrodes and extended voltage window. J Energy Storage 100:113617. https://doi.org/10.1016/j.est.2024.113617